# An extension of the approximate component mode synthesis method to the heterogeneous Helmholtz equation

Giammatteo, Elena; Heinlein, Alexander; Schlottbom, Matthias

**DOI**
10.1093/imanum/drae076

**Publication date**
2024

**Document Version**
Final published version

**Published in**
IMA Journal of Numerical Analysis

*IMA Journal of Numerical Analysis* (2024) **00**, 1–36
https://doi.org/10.1093/imanum/drae076

# An extension of the approximate component mode synthesis method to the heterogeneous Helmholtz equation

ELENA GIAMMATTEO
*Department of Applied Mathematics, University of Twente, P.O. Box 217, 7500 AE Enschede, The Netherlands*

ALEXANDER HEINLEIN
*Delft Institute of Applied Mathematics, Delft University of Technology, Mekelweg 4, 2628 CD Delft, The Netherlands*

AND

MATTHIAS SCHLOTTBOM*
*Department of Applied Mathematics, University of Twente, P.O. Box 217, 7500 AE Enschede, The Netherlands*
*Corresponding author: m.schlottbom@utwente.nl

[Received on 2 October 2023; revised on 3 September 2024]

In this work, we propose and analyze an extension of the approximate component mode synthesis (ACMS) method to the two-dimensional heterogeneous Helmholtz equation. The ACMS method has originally been introduced by Hetmaniuk and Lehoucq as a multiscale method to solve elliptic partial differential equations. The ACMS method uses a domain decomposition to separate the numerical approximation by splitting the variational problem into two independent parts: local Helmholtz problems and a global interface problem. While the former are naturally local and decoupled such that they can be easily solved in parallel, the latter requires the construction of suitable local basis functions relying on local eigenmodes and suitable extensions. We carry out a full error analysis of this approach focusing on the case where the domain decomposition is kept fixed, but the number of eigenfunctions is increased. The theoretical results in this work are supported by numerical experiments verifying algebraic convergence for the method. In certain, practically relevant cases, even super-algebraic convergence for the local Helmholtz problems can be achieved without oversampling.

*Keywords*: multiscale method; approximate component mode synthesis (ACMS); Helmholtz equation; heterogeneous media; high-frequency.

## 1. Introduction

In this paper, we propose and analyze a multiscale method for the heterogeneous Helmholtz equation

$$-\operatorname{div}(a\nabla u) - \kappa^2 u = f \quad \text{in } \Omega, \tag{1.1}$$

$$a\partial_n u - i\omega\beta u = g \quad \text{on } \Gamma_R, \tag{1.2}$$

$$u = 0 \quad \text{on } \Gamma_D, \tag{1.3}$$

in a plane region $\Omega \subset \mathbb{R}^2$. The boundary of $\Omega$ is decomposed into sets $\Gamma_D$ and $\Gamma_R$ modeling, respectively, Dirichlet boundary conditions and impedance boundary conditions described by the function $g$. The real-valued function $\beta$ is related to transmission and reflection of the wave described by $u$. Material properties of the background medium occupying $\Omega$ are described by the coefficient functions $a$ and $c$. Denoting the positive angular frequency as $\omega$, the wavenumber is given by $\kappa = \omega/c$ and any interior sources are modeled by the function $f$. Heterogeneous Helmholtz equations have many applications, such as modeling the propagation of light in photonic crystals, where $u$ is related to either the transverse-electric or the transverse-magnetic field Joannopoulos *et al.* (2008), or seismic imaging Bourgeous *et al.* (1991); Wang *et al.* (2011).

### 1.1 *Literature overview*

Numerical simulations of the Helmholtz equation are challenging due to the highly oscillatory behavior of the solution, in particular, in the case of a high wavenumber $\kappa$. The differential operator in the equation is indefinite, which may lead to stability issues for standard discretization approaches such as the classical finite element method (FEM). In order to resolve the oscillatory behavior of the solution, a wavenumber-dependent mesh size of $\mathcal{O}(1/\kappa)$ is required. Moreover, the FEM solution suffers from the pollution error in general, i.e., the ratio of the errors of the Galerkin solution and the best approximation grows with the wavenumber $\kappa$ (Babuška *et al.*, 1995, Theorem 2.6), Babuška & Sauter (1997). To obtain accurate FEM solutions, a much smaller mesh size $h$ satisfying $\kappa^3 h^2 = \mathcal{O}(1)$ has to be employed Deraemaeker *et al.* (1999); see also (Graham & Sauter, 2019, Theorem 4.5) where a similar condition is derived.

In order to overcome the pollution effect, higher-order methods can be employed: in particular, for the *hp*-FEM, quasi-optimality has been proved in Melenk & Sauter (2010, 2011) under the conditions that the polynomial degree $p$ is at least $\mathcal{O}(\log \kappa)$ and that $\kappa h/p$ is sufficiently small. In Chaumont-Frelet & Nicaise (2020) and Lafontaine *et al.* (2022), similar results have been achieved for the heterogeneous Helmholtz equation with piecewise smooth coefficients; however, to the authors' knowledge, no theory for rough coefficients is available yet.

Multiscale discretization approaches can be very efficient for problems with heterogeneous or non-smooth coefficients, especially if the variations are on a much smaller scale than the size of the computational domain. While for classical higher-order FEMs, fine-scale coefficient variations have to be resolved by mesh elements, multiscale methods are typically defined on a coarser grid, and fine-scale variations are handled via adapted basis functions; those basis functions are typically computed locally using a fine-scale mesh. Hence, systems resulting from multiscale methods are often smaller by orders of magnitude.

In recent years, many multiscale discretization methods have been developed and applied to the heterogeneous Helmholtz equation; for a review on numerical homogenization techniques, also addressing their application to Helmholtz problems, see Altmann *et al.* (2021). The localized orthogonal decomposition (LOD) method, introduced in Henning & Målqvist (2014) and Målqvist & Peterseim (2014), has successfully been applied to heterogeneous Helmholtz problems with high wavenumbers Brown *et al.* (2017); Peterseim (2017); Peterseim & Verfürth (2020). The LOD relies on a partition of the domain with coarse elements of size $H$, and basis functions that are computed using local oversampling domains of size $\ell H$. The approximation error is then bounded by $\mathcal{O}(H + \gamma^\ell)$ for some $0 < \gamma < 1$ assuming the resolution condition $H\kappa \ll 1$ and $\log(\kappa)/\ell$ bounded (Peterseim, 2017, Theorem 5.5). More recently, even super-exponential convergence of the localization error could be shown for a variant of the LOD method in Freese *et al.* (2021).

The heterogeneous multiscale method Abdulle *et al.* (2003); Abdulle & Vanden-Eijnden (2012), which relies on local periodicity of the media, has been extended to Helmholtz problems in Ohlberger & Verfurth (2018). The authors show quasi-optimality in terms of a wave-number dependent quasi-optimality constant.

Other multiscale discretization approaches are multiscale FEM (MsFEM) Babuška & Osborn (1983); Babuška *et al.* (1994); Hou & Wu (1997); see also, e.g., Efendiev & Hou (2009) for an overview on MsFEM. Nearly exponential error decay for the Helmholtz equation has been achieved in Ma *et al.* (2023), using similar ideas as in the multiscale generalized finite element method, first described in Efendiev *et al.* (2013). In a recent work, Chen, Hou and Wang Chen *et al.* (2023) extended ideas from elliptic equations Hetmaniuk & Lehoucq (2010); Hetmaniuk & Klawonn (2014); Chen *et al.* (2021) to the heterogeneous Helmholtz equation. The method in Chen *et al.* (2023) decomposes the solution into a microscale part and a macroscale part. The errors of the two parts are bounded by $\mathcal{O}(H)$ and $\mathcal{O}(H\ \exp(-I_e^{1/(d+1)-\varepsilon}))$, respectively, where $\varepsilon > 0$, $d$ is the space dimension and $I_e$ denotes the number of local basis functions associated to the edges of a coarse partition with mesh size $H$. These local basis functions are computed by local oversampling.

In domain decomposition methods, multiscale discretizations are also used as coarse spaces to construct preconditioners which are robust with respect to heterogeneous coefficients; see, e.g., Aarnes & Hou (2002); Gander *et al.* (2015); Heinlein *et al.* (2019); Heinlein & Smetana (2022) for applications to scalar elliptic problems, or Buck *et al.* (2013) for linear elasticity problems. For the application to heterogeneous Helmholtz problems, see, for instance, Conen *et al.* (2014), Gong *et al.* (2020) and Bootland *et al.* (2022).

Let us also refer to Wang *et al.* (2011) for an optimized parallel implementation of a direct solver based on local Schur complements on a hierarchy of domain decompositions reducing the number of low-rank compression operations compared with other structured direct solvers; see Liu *et al.* (2022) for a recent work in the context of elliptic equations. Finally, multigrid methods for the heterogeneous Helmholtz problem have been analyzed; see, e.g., Erlangga *et al.* (2006).

In this work, we consider an extension of the approximate component mode synthesis (ACMS) method to Helmholtz problems. The ACMS method has been introduced by Hetmaniuk and Lehoucq in Hetmaniuk & Lehoucq (2010) as a multiscale discretization for scalar elliptic problems with heterogeneous coefficient functions. It is based on the early component mode synthesis (CMS) method Hurty (1960); Craig & Bampton (1968), which uses a decomposition of the global approximation space into independent local subspaces and an interface space. The basis functions are defined as eigenmodes of corresponding generalized eigenvalue problems. The global support of the interface basis functions leads to high computational cost for their construction as well as a dense matrix structure of the interface problem. Hence, the practicability and potential for parallelization of CMS method are rather limited. Therefore, the ACMS method was introduced in order to improve the CMS approach: instead of global interface modes, functions with local support are employed. The basis functions incorporate heterogeneities of the model problem; notably, besides edge modes, this framework uses vertex basis functions of MsFEM Hou & Wu (1997); Efendiev & Hou (2009); Buck *et al.* (2013) type. Since the ACMS discretization uses problem-specific shape functions with local support, it can therefore be considered a special finite element method (SFEM) Babuška *et al.* (1994), and it also fits into the framework of the generalized finite element method Babuška *et al.* (2004). In contrast to other multiscale approaches, such as those previously mentioned Freese *et al.* (2021); Chen *et al.* (2023); Ma *et al.* (2023), the ACMS method of Hetmaniuk & Lehoucq (2010) is based on a non-overlapping domain decomposition and does not use local oversampling. Furthermore, we note that, although the current method as well as the one of Chen *et al.* (2023) rely on a similar decomposition of the solution in a

Helmholtz-harmonic and bubble part, we can compute these two contributions in parallel, while they are computed sequentially in Chen *et al.* (2023). This is due to the fact that the basis functions defined in Chen *et al.* (2023) and the ones defined here enjoy different orthogonality properties with respect to the sesquilinear form of the Helmholtz problem; see (Chen *et al.*, 2023, Remark 3.3) and Section 3 below.

The ACMS method has been further investigated in Hetmaniuk & Klawonn (2014), where *a priori* error bounds and an *a posteriori* error indicator for the method have been derived, and in Heinlein *et al.* (2015), where a parallel implementation in PETSc based on the finite element tearing and interconnecting dual primal domain decomposition method as the parallel solver is presented. More recently, a robust spectral coarse space for Schwarz domain decomposition methods based on the ACMS discretization has been introduced in Heinlein *et al.* (2018); further related works on CMS and ACMS methods include Bourquin (1990, 1992) and Madureira & Sarkis (2018). Moreover, to the authors' best knowledge, preliminary, but unpublished work on the extension of the ACMS method to wave problems, has been carried out by Hetmaniuk and Johnson in the early 2010s.

As a multiscale discretization, the ACMS method seems to be well suited for approximating heterogeneous Helmholtz problems. As we will discuss in this work, since the eigenmodes of the Helmholtz and the Laplacian operator are the same if the wavenumber is constant, similar ACMS basis functions as in the Laplace case are suitable for the Helmholtz equation as well.

### 1.2 *Our contribution and outline*

In this paper, we extend the ACMS method to heterogeneous Helmholtz problems. In doing so, we slightly modify the construction of the edge modes and the extension operator. These modifications are required because the weak formulation of the considered Helmholtz problem does not lead to a symmetric positive definite formulation, contrary to the elliptic case, for which the ACMS method has been developed originally. In the elliptic case Hetmaniuk & Lehoucq (2010); Hetmaniuk & Klawonn (2014), the orthogonality of the basis functions with respect to the bilinear form follows in a straightforward way from the definition, which is also exploited in the error analysis. For the Helmholtz case, on the contrary, it is necessary to adjust the definition of the extension operator in order to keep the orthogonality property with respect to the problem's indefinite sesquilinear form and in order to be consistent with the error analysis. At the same time, we adapt the method to Robin boundary conditions equation (1.2). Moreover, we fully localize the construction of the edge basis functions by solving only a one-dimensional eigenvalue problem on each edge, while the corresponding eigenvalue problems in Hetmaniuk & Lehoucq (2010), Hetmaniuk & Klawonn (2014) and Heinlein *et al.* (2015) couple edges to adjacent subdomains; see Remark 1.

This allows us to perform a full error analysis focusing on fixing the domain decomposition and increasing the number of eigenmodes for tackling the local heterogeneities. This approach is motivated by applications from wave propagation in (quasi)-periodic media Joannopoulos *et al.* (2008), where our construction yields an accurate local model for the propagation of light within one unit cell, i.e., one subdomain in the domain decomposition. While the error analysis for the local sub-problems, for which we obtain similar *a posteriori* error bounds as in Hetmaniuk & Klawonn (2014) is rather simple, the error analysis for the interface problem is slightly more sophisticated. The analysis is based on the abstract framework of Graham & Sauter (2019), and relies in particular on the smallness of the so-called adjoint approximability constant; see Section 4 and, in particular, equation (4.10) below. In contrast to Graham & Sauter (2019), where $H^2(\Omega)$-regularity of the solution of the adjoint problem is required, we require $H^2$-regularity of the solution of the adjoint problem only in the vicinity of the interface of the domain decomposition. We show that, upon using sufficiently many (edge) eigenmodes, the adjoint

approximability constant can be made arbitrarily small, and we provide an explicit scaling relation for the required number of edge modes in terms of frequency $\omega$. Moreover, we obtain cubic ($\mathcal{O}(I_e^{-3})$) and quadratic ($\mathcal{O}(I_e^{-2})$) convergence in the $L^2$- and $H^1$-norms, respectively, in terms of edge modes.

Finally, we present a detailed numerical study of the method using a flexible implementation that, unlike in the numerical results for the ACMS method shown in previous works, also allows for unstructured meshes and domain decompositions.

The paper is organized as follows: we introduce the necessary preliminaries for defining and analyzing the ACMS method for Helmholtz problems in Section 2. In particular, we show the variational formulation of the Helmholtz equation, recall the well-posedness results of Graham & Sauter (2019), and illustrate the underlying domain decomposition and function spaces of the ACMS discretization. Then, in Section 3, we present our new variant of the ACMS method for Helmholtz problems along with some theoretical properties. The error analysis of the ACMS method is carried out in Section 4. Finally, we describe our numerical results in Section 5 and conclude with some final remarks.

## 2. Preliminaries

In the following, we introduce the functional analytic setting and recall well-posedness results for the heterogeneous Helmholtz equation. Furthermore, we introduce the domain decomposition used in the ACMS method.

### 2.1 *Variational formulation of the Helmholtz equation*

We denote by $L^2(\Omega)$ the Lebesgue space of square-integrable functions $v : \Omega \to \mathbb{C}$ with inner product

$$(u, v)_\Omega = \int_\Omega u\,\bar{v}\,\mathrm{d}x,$$

and by $H^1(\Omega)$ the usual Sobolev space of functions in $L^2(\Omega)$ with square-integrable weak derivatives. We denote the associated norm as $\|\cdot\|_{L^2(\Omega)}$. Corresponding notation is used for other measurable sets besides $\Omega$. Furthermore, we indicate by $H^1_D(\Omega) \subset H^1(\Omega)$ functions with vanishing trace on $\Gamma_D \subset \partial\Omega$. Let us introduce the sesquilinear forms $\mathscr{A}, \mathscr{C} : H^1_D(\Omega) \times H^1_D(\Omega) \to \mathbb{C}$ defined by

$$\mathscr{A}(u, v) = \int_\Omega a\nabla u \cdot \nabla\bar{v}\,\mathrm{d}x, \tag{2.1}$$

$$\mathscr{C}(u, v) = \mathscr{A}(u, v) - (\kappa^2 u, v)_\Omega - i(\omega\beta u, v)_{\Gamma_R}. \tag{2.2}$$

Then the weak form of the Helmholtz problem (1.1), (1.2), (1.3) and its adjoint are

$$\text{Find } u \in H^1_D(\Omega): \quad \mathscr{C}(u, v) = F(v), \quad \text{for all } v \in H^1_D(\Omega), \tag{2.3}$$

$$\text{Find } z \in H^1_D(\Omega): \quad \mathscr{C}(v, z) = G(v), \quad \text{for all } v \in H^1_D(\Omega). \tag{2.4}$$

Here, $F : H^1_D(\Omega) \to \mathbb{C}$ and $G : H^1_D(\Omega) \to \mathbb{C}$, defined by

$$F(v) = (f, v)_\Omega + (g, v)_{\Gamma_R}, \tag{2.5}$$

$$G(v) = (v,f)_\Omega + (v, g)_{\Gamma_R}, \tag{2.6}$$

are antilinear and linear functionals on $H^1_D(\Omega)$, respectively.

### 2.2 *Well-posedness of the Helmholtz equation*

We recall the well-posedness theory for the Helmholtz equation presented in Graham & Sauter (2019). Thus, we deem the following assumptions valid throughout the paper without explicitly mentioning it:

ASSUMPTION 2.1. (i) $\Omega \subset \mathbb{R}^2$ is a connected polygonal domain with piecewise $C^2$ boundary with strictly convex angles. Its boundary can be decomposed as $\partial\Omega = \overline{\Gamma_R} \cup \overline{\Gamma_D}$ into relatively open disjoint subsets $\Gamma_R, \Gamma_D \subset \partial\Omega$. The angle between a segment in $\Gamma_D$ and $\Gamma_R$ is smaller than $\pi/2$. (ii) The source terms satisfy $f \in L^2(\Omega)$ and $g \in H^{1/2}(\Gamma_R)$. (iii) The coefficient functions $a, c \in L^\infty(\Omega)$ are uniformly positive, i.e., $a_{\min} \le a(x) \le a_{\max}$ and $c_{\min} \le c(x) \le c_{\max}$ for a.e. $x \in \Omega$, where $a_{\min}, c_{\min}, a_{\max}, c_{\max}$ are positive constants. Recall that the coefficient function $c$ is such that $\kappa = \omega/c$, where $\omega$ is the angular frequency. (iv) $\beta \in L^\infty(\Gamma_R)$ with $\mathrm{meas}(\mathrm{supp}(\beta)) > 0$ and either $\beta > 0$ or $\beta < 0$.

The analysis employs the norm $\|u\|^2_{\mathscr{B}} = \mathscr{B}(u, u)$ induced by the sesquilinear form

$$\mathscr{B}(u, v) = \mathscr{A}(u, v) + (\kappa^2 u, v)_\Omega, \tag{2.7}$$

defined for $u, v \in H^1_D(\Omega)$; see Graham & Sauter (2019); Chen *et al.* (2023); Ma *et al.* (2023). In (Graham & Sauter, 2019, Thm. 2.4), the following result is proved. We recall parts of the proof to show robustness of the constant $C_{\mathscr{C}}$ for high-frequencies $\omega \to \infty$.

THEOREM 2.2. (i) For all $u, v \in H^1_D(\Omega)$, it holds that

$$|\mathscr{C}(u, v)| \le C_{\mathscr{C}} \|u\|_{\mathscr{B}} \|v\|_{\mathscr{B}}, \tag{2.8}$$

with constant $C_{\mathscr{C}} = 1 + C_\Omega \beta_{\max} \max\left\{a_{\min}^{-1}, \frac{1+\omega}{\omega} c_{\max}\right\}$ and constant $C_\Omega$ depending only on $\Omega$. (ii) There exist unique solutions of equation (2.3), (2.4).

(iii) If $g = 0$ in equation (2.3) and 2.4, then there exists a constant $C_{\mathrm{stab}} = C_{\mathrm{stab}}(a, c, \omega, \Omega)$ such that the corresponding solutions $u$ and $z$ satisfy:

$$\|u\|_{\mathscr{B}} \le C_{\mathrm{stab}} \|f\|_{L^2(\Omega)}, \quad \|z\|_{\mathscr{B}} \le C_{\mathrm{stab}} \|f\|_{L^2(\Omega)}. \tag{2.9}$$

*Proof.* We only derive the constant $C_{\mathscr{C}}$, for the other statements, see (Graham & Sauter, 2019, Thm. 2.4). An application of the Cauchy–Schwarz inequality to equation (2.2) yields that

$$|\mathscr{C}(u, v)| \le \|u\|_{\mathscr{B}} \|v\|_{\mathscr{B}} + (\omega|\beta|u, u)^{1/2}_{\Gamma_R} (\omega|\beta|v, v)^{1/2}_{\Gamma_R}.$$

The trace inequality yields a constant $C_\Omega > 0$, depending on $\Omega$ such that (Grisvard, 2011, p. 41)

$$\begin{aligned}(\omega|\beta|u,u)_{\Gamma_R} &\leq C_\Omega \beta_{\max}\left(\omega\|u\|_{L^2(\Omega)}\|\nabla u\|_{L^2(\Omega)} + \omega\|u\|^2_{L^2(\Omega)}\right)\\ &\leq C_\Omega \beta_{\max}\left(\frac{c_{\max}}{\sqrt{a_{\min}}}\|\frac{\omega}{c}u\|_{L^2(\Omega)}\|\sqrt{a}\nabla u\|_{L^2(\Omega)} + \frac{c^2_{\max}}{\omega}\|\frac{\omega}{c}u\|^2_{L^2(\Omega)}\right)\\ &\leq C_\Omega \beta_{\max}\max\left\{\frac{1}{a_{\min}}, \frac{1+\omega}{\omega}c^2_{\max}\right\}\|u\|^2_{\mathscr{B}},\end{aligned}$$

from which (2.8) follows. □

Given Assumption 2.1, it follows that the solution $u$ of equation (2.3) satisfies $\nabla u \in L^p(\Omega)$ for some $p > 2$; cf. Gröger (1989). By invoking the Sobolev embedding theorem (Adams, 1975, p. 97), we thus have that $u$ is Hölder continuous in $\bar{\Omega}$ with exponent $1 - 2/p$. Condition (i) in Assumption 2.1 is used in Section 4.4 below to verify higher regularity of the solution of the dual problem; see Shamir (1968) for a counterexample if (i) is not satisfied.

### 2.3 *Decomposition of the computational domain*

Let $\{\Omega_j\}_{j=1}^J$ denote a conforming decomposition of $\Omega$ into $J$ non-overlapping domains $\Omega_j$ with piecewise smooth boundaries. Furthermore, let

$$\Gamma = \bigcup_{j=1}^{J} \partial\Omega_j \setminus \overline{\Gamma_D}$$

denote the domain decomposition interface and $\mathscr{E}$ the set of all edges of the domain decomposition, where each edge $e$ is a relatively open set with either $\bar{e} = \partial\Omega_i \cap \partial\Omega_j$ for some $i \neq j$ or $e \subset \Gamma_R \cap \partial\Omega_i$ for some $i$. Furthermore, let $\mathscr{V} = \{p \in \Gamma\} = \Gamma \setminus \cup_{e\in\mathscr{E}} e$ be the set of points connecting adjacent edges, which we also refer to as the vertices of the domain decomposition.

### 2.4 *Function spaces*

The Lions–Magenes space $H^{1/2}_{00}(e)$ is defined as an interpolation space between $L^2(e)$ and $H^1_0(e)$ (Lions & Magenes, 1972, Ch. 1, Thm. 11.7). Therefore, it holds that $H^1_0(e) \subset H^{1/2}_{00}(e)$ densely (Lions & Magenes, 1972, p. 10). We have the following interpolation inequality

$$\|\eta\|_{H^{1/2}_{00}(e)} \leq C\|\eta\|^{1/2}_{L^2(e)}\|\eta\|^{1/2}_{H^1_0(e)} \tag{2.10}$$

for all $\eta \in H^1_0(e)$ (Lions & Magenes, 1972, Proposition 23, p. 19). The space $H^{1/2}(e)$ is defined as the interpolation space between $H^1(e)$ and $L^2(e)$; see (Lions & Magenes, 1972, Ch. 1, Thm. 9.6). In view of (Lions & Magenes, 1972, Ch. 1, Thm. 11.7), if $e \subset \partial\Omega_j$ for some $1 \leq j \leq J$, functions in $H^{1/2}_{00}(e)$ can be extended continuously by zero to functions in $H^{1/2}(\partial\Omega_j)$. Here, $H^{1/2}(\partial\Omega_j)$ denotes the space of traces of functions in $H^1(\Omega_j)$; cf. (Lions & Magenes, 1972, Ch. 1, Thm. 8.3). Lastly, by $H^{1/2}_D(\Gamma)$ we denote the space of traces on $\Gamma$, i.e., $v \in H^{1/2}_D(\Gamma)$ if there exist $u \in H^1_D(\Omega)$ such that $u_{|\Gamma} = v$.

## 3. ACMS method

The ACMS method introduced in Hetmaniuk & Lehoucq (2010) relies on an orthogonal splitting of $H^1(\Omega)$ into interface functions $H_D^{1/2}(\Gamma)$ and local functions $H_0^1(\Omega_j), j = 1, \ldots, J$, and on the availability of basis functions with local support; while functions in $H_0^1(\Omega_j)$ generally have local support, interface basis functions with local support are constructed based on the edges and vertices that form $\Gamma$. In Hetmaniuk & Lehoucq (2010), orthogonality is characterized by the bilinear form associated to the elliptic problem. The basic idea of our extension of the ACMS method to Helmholtz problems is similar, but 'orthogonality' is measured with respect to the sequilinear form $\mathscr{C}$ defined in equation (2.2), which is not an inner product in general. Below we will construct spaces

$$V_S := V_{B,S_B} \oplus V_{\Gamma,S_\Gamma} \tag{3.1}$$

that are either associated to the subdomains $\Omega_j$ or to the interface $\Gamma$. In particular, the corresponding basis functions have local support and can be built locally. We now discuss the construction of the bubble space $V_{B,S_B}$ and the interface space $V_{\Gamma,S_\Gamma}$ in detail.

### 3.1 *Bubble space*

Let us define the local sesquilinear form $\mathscr{A}_j : H^1(\Omega_j) \times H^1(\Omega_j) \to \mathbb{C}$ as in equation (2.1), but with domain of integration $\Omega_j$ instead of $\Omega$. Since $\mathscr{A}_j$ is Hermitian, we can consider the eigenproblems: for $j = 1, ..., J$ and $i \in \mathbb{N}$, find $(b_i^j, \lambda_i^j) \in H_0^1(\Omega_j) \times \mathbb{R}$ such that

$$\mathscr{A}_j(b_i^j, v) = \lambda_i^j (\kappa^2 b_i^j, v)_{\Omega_j} \quad \text{for all } v \in H_0^1(\Omega_j). \tag{3.2}$$

Standard theory ensures that the eigenfunctions $\{b_j^i\}_i$ form an orthogonal basis for $H_0^1(\Omega_j)$ with respect to $\mathscr{A}_j$ and can be normalized to an orthonormal basis for $L^2(\Omega_j)$ with weighted inner product $(\kappa^2 u, v)_{\Omega_j}$, and that $\lambda_i^j > 0$. Furthermore, we may assume that the eigenvalues $\lambda_i^j$ are ordered non-decreasingly, i.e., $\lambda_i^j \leq \lambda_l^j$ for $i \leq l$. By definition $\kappa(x) = \omega/c(x)$, and, hence, the numbers $\lambda_i^j \omega^2$ are eigenvalues of a corresponding eigenproblem that is independent of $\omega$. As such, $\lambda_i^j \omega^2$ is independent of $\omega$. If $c(x)$ is constant, the bubble functions are defined as in the elliptic case in Hetmaniuk & Lehoucq (2010). In slight abuse of notation, we may denote by $b_i^j \in H_0^1(\Omega)$ also the extension of $b_i^j \in H_0^1(\Omega_j)$ by zero outside of $\Omega_j$ and we call these *bubble functions*. Associated to the partition $\{\Omega_j\}_j$ of $\Omega$, let us introduce the infinite-dimensional bubble space

$$V_B = \bigoplus_{j=1}^{J} V^j, \qquad \text{with } V^j = \operatorname{span}\{ b_i^j \,:\, i \in \mathbb{N}\}. \tag{3.3}$$

Let $S_B = (I_1, \ldots, I_J) \in \mathbb{N}^J$ be a multi-index. Then, the finite-dimensional bubble space employed in the ACMS method is defined by

$$V_{B,S_B} = \bigoplus_{j=1}^{J} V_{I_j}^j, \qquad \text{with } V_{I_j}^j = \operatorname{span}\{ b_i^j \,:\, 1 \leq i \leq I_j\}. \tag{3.4}$$

### 3.2 *Solvability of local Helmholtz problems*

The interface space $V_{\Gamma,S_\Gamma}$ introduced below relies on the proper extension of functions defined on the interface $\Gamma$. The extension relies on the solvability of local Helmholtz problems with homogeneous Dirichlet boundary conditions. Therefore, in the rest of the manuscript, we additionally assume the following:

ASSUMPTION 3.1. For all $j = 1, \dots, J$ and for all $i \in \mathbb{N}$, let $\lambda_i^j \neq 1$.

Assumption 3.1 might be justified by suitably adapting the partition $\{\Omega_j\}_j$ such that the spectrum of the corresponding differential operator in equation (3.2) does not include the value 1: the eigenvalues $\lambda_i^j$ depend on the size of $\Omega_j$, and they grow if $\Omega_j$ is suitably made smaller, cf. (3.10) for the corresponding scaling behavior of eigenvalues for one-dimensional eigenvalue problems. As noted in Section 3.1, the numbers $\lambda_i^j \omega^2$ are independent of $\omega$. Hence, the suitable adjustment of $\{\Omega_j\}$ that guarantees that Assumption 3.1 holds, depends on the frequency $\omega$. Similar assumptions have been used, e.g., in (Freese *et al.*, 2021, Assumption 4.2) or (Chen *et al.*, 2023, Assumption 1), to guarantee coercivity of the local Helmholtz problems. Next, we establish well-posedness of the local Helmholtz problems under the conditions of Assumption 3.1.

LEMMA 3.2. For $\beta^j = \inf_{i\in\mathbb{N}}\{|\lambda_i^j - 1|/(\lambda_i^j + 1)\} > 0$, the following estimates hold:

$$\inf_{u\in H_0^1(\Omega_j)} \sup_{v\in H_0^1(\Omega_j)} \frac{\mathscr{A}_j(u,v) - (\kappa^2 u, v)_{\Omega_j}}{\|u\|_{\mathscr{B}}\|v\|_{\mathscr{B}}} \geq \beta^j,$$

$$\inf_{v\in H_0^1(\Omega_j)} \sup_{u\in H_0^1(\Omega_j)} \frac{\mathscr{A}_j(u,v) - (\kappa^2 u, v)_{\Omega_j}}{\|u\|_{\mathscr{B}}\|v\|_{\mathscr{B}}} \geq \beta^j.$$

*Proof.* Assumption 3.1 implies that $\beta^j > 0$. Let $u \in H_0^1(\Omega_j)$ be given. Since $\{b_i^j\}_i$ is a basis of $H_0^1(\Omega_j)$, we have that $u = \sum_{i=1}^\infty u_i b_i^j$ with $u_i = (\kappa^2 u, b_i^j)_{\Omega_j}$. Let $v = \sum_{i=1}^\infty \operatorname{sgn}(\lambda_i^j - 1) u_i b_i^j$. We note that

$$\|u\|_{\mathscr{B}}^2 = \sum_{i=1}^\infty (\lambda_i^j + 1)|u_i|^2,$$

and $\|v\|_{\mathscr{B}} = \|u\|_{\mathscr{B}}$. Then we have that

$$\mathscr{A}_j(u,v) - (\kappa^2 u, v)_{\Omega_j} = \sum_{i=1}^\infty |\lambda_i^j - 1||u_i|^2 \geq \inf_{i\in\mathbb{N}} \frac{|\lambda_i^j - 1|}{\lambda_i^j + 1} \|u\|_{\mathscr{B}}^2.$$

Hence, the first inequality follows. The second inequality follows similarly. □

### 3.3 *A harmonic extension operator*

In order to define the interface space, we need an extension from $\Gamma$ to $\Omega$, which is obtained by combining the extensions of functions from $\partial\Omega_j$ to $\Omega_j$.

For a given $\tau \in H^{1/2}(\partial\Omega_j)$, let $\tilde{\tau} \in H^1(\Omega_j)$ be any function satisfying $\tilde{\tau}_{|\partial\Omega_j} = \tau$. Then we indicate by $\tilde{\tau}_0 \in H^1_0(\Omega_j)$ the solution to

$$\mathscr{A}_j(\tilde{\tau}_0, v) - (\kappa^2\tilde{\tau}_0, v)_{\Omega_j} = -\left(\mathscr{A}_j(\tilde{\tau}, v) - (\kappa^2\tilde{\tau}, v)_{\Omega_j}\right) \quad \text{for all } v \in H^1_0(\Omega_j), \tag{3.5}$$

which is uniquely defined by Lemma 3.2. We introduce the local Helmholtz-harmonic extension $E^j : H^{1/2}(\partial\Omega_j) \to H^1(\Omega_j)$ by setting $E^j\tau = \tilde{\tau} + \tilde{\tau}_0$.

LEMMA 3.3. The extension operator $E^j : H^{1/2}(\partial\Omega_j) \to H^1(\Omega_j)$ is bounded, that is,

$$\|E^j\tau\|_{\mathscr{B}} \leq (1 + 1/\beta^j)\|\tilde{\tau}\|_{\mathscr{B}}, \tag{3.6}$$

where $\tilde{\tau} \in H^1(\Omega_j)$ is any extension of $\tau \in H^{1/2}(\partial\Omega_j)$.

*Proof.* We estimate the right-hand side in equation (3.5) by $\|\tilde{\tau}\|_{\mathscr{B}}\|v\|_{\mathscr{B}}$. Then, Lemma 3.2 yields that $\|\tilde{\tau}_0\|_{\mathscr{B}} \leq \|\tilde{\tau}\|_{\mathscr{B}}/\beta^j$, and the assertion follows. □

We note the following orthogonality relation, which is a crucial property for the construction of the ACMS spaces: for $\tau \in H^{1/2}(\partial\Omega_j)$ and for all bubble functions $b^j_i \in H^1_0(\Omega_j)$, we have

$$\mathscr{A}_j(E^j\tau, b^j_i) - (\kappa^2 E^j\tau, b^j_i)_{\Omega_j} = 0. \tag{3.7}$$

Next, we construct extensions from the local edges and the interface. We assume that $e = \partial\Omega_j \cap \partial\Omega_i \in \mathscr{E}$ is a common edge of $\Omega_i$ and $\Omega_j$. Let $\tau \in H^{1/2}_D(\Gamma)$, which, by restriction, implies $\tau \in H^{1/2}(\partial\Omega_j)$ and $\tau \in H^{1/2}(\partial\Omega_i)$. Since $(E^j\tau)_{|e} = \tau_{|e} = (E^i\tau)_{|e}$, we can introduce the extension operator $E^\Gamma : H^{1/2}_D(\Gamma) \to H^1_D(\Omega)$ by $(E^\Gamma\tau)_{|\Omega_j} = E^j\tau_{|\partial\Omega_j}$, for all $j = 1, \ldots, J$. Moreover, we define $E^e : H^{1/2}_{00}(e) \to H^1_D(\Omega)$ via $E^e\tau = E^\Gamma E^e_0\tau$, where $E^e_0 : H^{1/2}_{00}(e) \to H^{1/2}_D(\Gamma)$ denotes the extension by zero to the interface $\Gamma$.

### 3.4 *Vertex based approximation space*

For any $p \in \mathscr{V}$, let $\varphi_p : \Gamma \to \mathbb{R}$ denote a piecewise harmonic function, that is, $\Delta_e\varphi_{p|e} = 0$ for all $e \in \mathscr{E}$, with $\Delta_e$ indicating the Laplace operator along the edge $e \in \mathscr{E}$, and $\varphi_p(q) = \delta_{p,q}$ for all $p, q \in \mathscr{V}$. Note that the support of $\varphi_p$ consists of all edges which share the vertex $p$ and is, therefore, local. In turn, $E^\Gamma\varphi_p$ is supported on all subdomains $\Omega_j$ that share the vertex $p$. If all edges $e \in \mathscr{E}$ are straight line segments, then $\varphi_p$ is a piecewise linear function on $\Gamma$, similar to Hetmaniuk & Lehoucq (2010). The choice of $\Delta_e$ here is motivated by the error analysis in Section 4.3. The vertex based space is then defined by linear combinations of corresponding extensions,

$$V_{\mathscr{V}} = \text{span}\{E^\Gamma\varphi_p \ : \ p \in \mathscr{V}\}.$$

For our error analysis, we will employ the nodal interpolant

$$I_{\mathscr{V}}v = \sum_{p\in\mathscr{V}} v(p)\varphi_p, \tag{3.8}$$

which is well-defined for functions $v : \overline{\Omega} \to \mathbb{C}$ that are continuous in all $p \in \mathcal{V}$. Note that $I_{\mathcal{V}}$ can be applied to the solution $u \in H^1_D(\Omega) \cap W^{1,p}(\Omega)$ to equation (2.3); see the comments at the end of Section 2.2.

### 3.5 *Interface space*

Let us consider $e \in \mathcal{E}$ and denote by $\partial_e$ the tangential derivative, i.e., differentiation along $e$. We define the edge modes as solutions to the following weak formulation of the edge-Laplace eigenvalue problems: for each $e \in \mathcal{E}$, find $(\tau_i^e, \lambda_i^e) \in H^1_0(e) \times \mathbb{R}$, $i \in \mathbb{N}$, such that

$$(\partial_e \tau_i^e, \partial_e \eta)_e = \lambda_i^e (\tau_i^e, \eta)_e \quad \text{for all } \eta \in H^1_0(e). \tag{3.9}$$

Standard theory ensures that the eigenfunctions $\{\tau_i^e\}_i$ form an orthogonal basis for $H^1_0(e)$ and can be normalized to an orthonormal basis for $L^2(e)$. We may again assume that the eigenvalues $\lambda_j^e > 0$ are ordered increasingly. Moreover, we note that the asymptotic behavior of the eigenvalues is (Courant & Hilbert, 1953, p. 415)

$$\lambda_i^e \sim \left(\frac{i\pi}{|e|}\right)^2. \tag{3.10}$$

Remark 1. Let us mention that the definition of the edge modes here requires the solution of local eigenvalue problems only on the edges and differs from the definition in the classical ACMS method of Hetmaniuk & Lehoucq (2010); Hetmaniuk & Klawonn (2014), where the authors solve eigenvalue problems involving the extension operator, resulting in problems on two neighboring subdomains; see, e.g., (Hetmaniuk & Lehoucq, 2010, Equation (3.4)).

The corresponding infinite-dimensional interface space is

$$V_\Gamma = V_{\mathcal{V}} + \sum_{e \in \mathcal{E}} E^e V^e, \quad V^e = \operatorname{span}\{\tau_i^e \,:\, i \in \mathbb{N}\}. \tag{3.11}$$

Note that each function in $E^e V^e$ has local support inside the two subdomains adjacent to $e$. Choosing $I_e \in \mathbb{N}$, $e \in \mathcal{E}$, we introduce the $L^2(e)$-projection $P^e_{I_e} : L^2(e) \to V^e$ defined by

$$P^e_{I_e} v = \sum_{j=1}^{I_e} (v, \tau_j^e)_e \tau_j^e, \tag{3.12}$$

and denote the range of $P^e_{I_e}$ by $V^e_{I_e}$. Collecting the indices $I_e$ in a multi-index $S_\Gamma$, we define the finite-dimensional interface space by

$$V_{\Gamma, S_\Gamma} = V_{\mathcal{V}} + \sum_{e \in \mathcal{E}} E^e V^e_{I_e}, \tag{3.13}$$

which, together with equation (3.4), completes the construction of the ACMS approximation space in equation (3.1). We now give some well-known interpolation error estimates; see, e.g., (Larsson & Thomée, 2003, p. 83). We recall the proofs for convenience of the reader.

LEMMA 3.4. For any $e \in \mathscr{E}$ and all $w \in H_0^1(e)$, it holds that

$$\|w - P_{I_e}^e w\|_{L^2(e)} \leq \frac{1}{\sqrt{\lambda_{I_e+1}^e}} \|w - P_{I_e}^e w\|_{H^1(e)}. \tag{3.14}$$

If, additionally, $w \in H_0^1(e) \cap H^2(e)$, then there exists a constant $C > 0$ such that

$$\|w - P_{I_e}^e w\|_{H^1(e)} \leq \frac{C}{\sqrt{\lambda_{I_e+1}^e}} \|\Delta_e w - P_{I_e}^e \Delta_e w\|_{L^2(e)}. \tag{3.15}$$

*Proof.* Since $\{\tau_j^e\}_j$ form an orthonormal basis of $L^2(e)$, we have that

$$\|w - P_{I_e}^e w\|_{L^2(e)}^2 = \sum_{j \geq I_e+1} |(w, \tau_j^e)_e|^2 \leq \frac{1}{\lambda_{I_e+1}^e} \|w - P_{I_e}^e w\|_{H^1(e)}^2,$$

which proves (3.14). By equation (3.9) and the Poincaré inequality, we similarly have that

$$\|w - P_{I_e}^e w\|_{H^1(e)}^2 \leq C_P \sum_{j \geq I_e+1} \lambda_j^e |(w, \tau_j^e)_e|^2.$$

Using the definition of $\tau_j^e$ in equation (3.9) again and performing integration by parts, we obtain

$$(w, \tau_j^e)_e = \frac{1}{\lambda_j^e} (\partial_e w, \partial_e \tau_j^e)_e = -\frac{1}{\lambda_j^e} (\Delta_e w, \tau_j^e)_e,$$

where we used that $w, \tau_j^e \in H_0^1(e)$. This concludes the proof of (3.15). □

LEMMA 3.5. Let $e \in \mathscr{E}$. Then, there exists a constant $C > 0$ such that

$$\inf_{v^e \in V_{I_e}^e} \|w - I_{\mathscr{V}} w - v^e\|_{H_{00}^{1/2}(e)} \leq \frac{C}{\sqrt{\lambda_{I_e+1}^e}} \|w\|_{H^{3/2}(e)} \tag{3.16}$$

for all $w \in H^{3/2}(e)$, with nodal interpolant $I_{\mathscr{V}} w$ defined in equation (3.8).

*Proof.* By continuity of the embedding $H^1(e) \hookrightarrow C^0(\overline{e})$, we have that the nodal interpolation operator $I_{\mathscr{V}}$ is bounded, i.e., $\|I_{\mathscr{V}} w\|_{H^1(e)} \leq C \|w\|_{H^1(e)}$ for all $w \in H^1(e)$. By choosing $v^e = 0$, we thus have the stability estimate

$$\inf_{v^e \in V_{I_e}^e} \|w - I_{\mathscr{V}} w - v^e\|_{H^1(e)} \leq C \|w\|_{H^1(e)} \quad \text{for all } w \in H^1(e). \tag{3.17}$$

Employing Lemma 3.4 and using that $w - I_{\mathcal{V}} w \in H_0^1(e)$, we also have that

$$\inf_{v^e \in V_{I_e}^e} \|w - I_{\mathcal{V}} w - v^e\|_{H^1(e)} \leq \frac{C}{\sqrt{\lambda_{I_e+1}^e}} \|w\|_{H^2(e)} \quad \text{for all } w \in H^2(e).$$

Therefore, we get by interpolation (Lions & Magenes, 1972, Thm. 5.1, Thm. 9.6) that

$$\inf_{v^e \in V_{I_e}^e} \|w - I_{\mathcal{V}} w - v^e\|_{H^1(e)} \leq \frac{C}{(\lambda_{I_e+1}^e)^{1/4}} \|w\|_{H^{3/2}(e)} \quad \text{for all } w \in H^{3/2}(e). \tag{3.18}$$

Employing equation (3.18) and Lemma 3.4 and recalling that the best-approximation is realized via the projection $P_{I_e}^e (w - I_{\mathcal{V}} w)$, we also have that

$$\inf_{v^e \in V_{I_e}^e} \|w - I_{\mathcal{V}} w - v^e\|_{L^2(e)} \leq \frac{1}{(\lambda_{I_e+1}^e)^{3/4}} \|w\|_{H^{3/2}(e)} \quad \text{for all } w \in H^{3/2}(e). \tag{3.19}$$

Therefore, by the interpolation inequality (2.10), the relations (3.18), (3.19) yield (3.16), which concludes the proof. □

The next result shows that $H_D^1(\Omega)$-functions can be approximated by bubble and interface functions. The proof of this statement is also the recipe to obtain quantitative error estimates in Section 4.3.

LEMMA 3.6. Let $V_B$ and $V_\Gamma$ be as in equation (3.3) and equation (3.11), respectively. Then it holds that $H_D^1(\Omega) = V_B \oplus V_\Gamma$.

*Proof.* Using a density argument, it is sufficient to show that any function $v \in H_D^1(\Omega) \cap C_0^\infty(\Omega \cup \Gamma_R)$ can be approximated by functions in $V_B \oplus V_\Gamma$. First note that $(v - E^\Gamma v_{|\Gamma})_{|\Omega_j} \in H_0^1(\Omega_j)$ for each $j = 1, ..., J$. Therefore, $v - E^\Gamma v_{|\Gamma} \in V_B$. It remains to show that $E^\Gamma v_{|\Gamma}$ can be approximated by functions in the interface space $V_\Gamma$. By continuity of $E^\Gamma$, it is sufficient to approximate $v_{|\partial\Omega_j}$ in $H^{1/2}(\partial\Omega_j)$. First, we subtract the nodal interpolant, and observe that $(v - I_{\mathcal{V}} v)_{|e} \in H_0^1(e) \subset H_{00}^{1/2}(e)$ for any $e \in \mathcal{E}$ such that $e \subset \partial\Omega_j$. Then, $\|v - I_{\mathcal{V}} v\|_{H^{1/2}(\partial\Omega_j)}$ can be localized to single edges $e \subset \partial\Omega_j$ as follows: define $w^e \in H^{1/2}(\partial\Omega_j)$ via $w^e = (v - I_{\mathcal{V}} v)_{|e}$ and $w^e = 0$ on $\partial\Omega_j \setminus e$. We observe that $v - I_{\mathcal{V}} v = \sum_{e \subset \partial\Omega_j} w^e$ on $\partial\Omega_j$. From (Grisvard, 2011, Lemma 1.3.2.6), we have that $\|w^e\|_{H^{1/2}(\partial\Omega_j)}$ is equivalent to $\|w^e\|_{H_{00}^{1/2}(e)}$. Since it holds $\|v - I_{\mathcal{V}} v\|_{H^{1/2}(\partial\Omega_j)} \leq \sum_{e \subset \partial\Omega_j} \|w^e\|_{H^{1/2}(\partial\Omega_j)} \leq C \sum_{e \subset \partial\Omega_j} \|w^e\|_{H_{00}^{1/2}(e)}$, the result follows from noting that $w_{|e}^e \in V^e$. □

## 4. Galerkin approximation

We start by observing that

$$\mathscr{C}(v_B, v_\Gamma) = \mathscr{A}(v_B, v_\Gamma) - (\kappa^2 v_B, v_\Gamma) - i(\omega\beta v_B, v_\Gamma)_{\Gamma_R} = 0, \tag{4.1}$$

for all $v_B \in V_B$ and $v_\Gamma \in V_\Gamma$, where we used equation (3.7) and that $v_B = 0$ on $\Gamma_R$. Similarly, $\mathscr{C}(v_\Gamma, v_B) = 0$. Since $u = u_B + u_\Gamma \in V_B \oplus V_\Gamma$ with $u_B = u - E^\Gamma u_{|\Gamma}$ and $u_\Gamma = E^\Gamma u_{|\Gamma}$, we thus obtain that

$$\mathscr{C}(u_B, v_B) = F(v_B) \quad \text{for all } v_B \in V_B \quad \text{and} \tag{4.2}$$

$$\mathscr{C}(u_\Gamma, v_\Gamma) = F(v_\Gamma) \quad \text{for all } v_\Gamma \in V_\Gamma. \tag{4.3}$$

Recalling that $V_S = V_{B,S_B} \oplus V_{\Gamma,S_\Gamma}$ has been defined in equation (3.1), with $V_{B,S_B} \subset V_B$ and $V_{\Gamma,S_\Gamma} \subset V_\Gamma$ defined in equation (3.4) and equation (3.13), respectively, the Galerkin approximations of (4.2)–(4.3) are split into two independent problems, namely a *bubble approximation*: find $u_{B,S} \in V_{B,S_B}$ such that

$$\mathscr{C}(u_{B,S}, v_{B,S}) = F(v_{B,S}) \quad \text{for all } v_{B,S} \in V_{B,S_B}; \tag{4.4}$$

and an *interface approximation*: find $u_{\Gamma,S} \in V_{\Gamma,S_\Gamma}$ such that

$$\mathscr{C}(u_{S,\Gamma}, v_{S,\Gamma}) = F(v_{S,\Gamma}) \quad \text{for all } v_{S,\Gamma} \in V_{\Gamma,S_\Gamma}. \tag{4.5}$$

The Galerkin problem (4.4) is well-posed under Assumption 3.1, while adjoint approximability is required to analyze the Galerkin problem (4.5); cf. Graham & Sauter (2019). In Theorem 4.6 below, we prove estimates for the adjoint approximability constant, ensuring that also (4.5) is well-posed as long as the number of edge modes is sufficiently large. In the following subsections, we present an error analysis for the two independent approximation problems (4.4), (4.5).

### 4.1 *Error estimates for the bubble approximation*

For the statement of the approximation result, let us introduce the $L^2$-projection $P^j_{I_j} : L^2(\Omega) \to V^j_{I_j}$, given by

$$P^j_{I_j} f = \sum_{i=1}^{I_j} (\kappa^2 f, b^j_i)_{\Omega_j} b^j_i. \tag{4.6}$$

The error analysis is then straight-forward, and the proof is given for convenience of the reader.

THEOREM 4.1. Assume $f \in L^2(\Omega)$ and set $f_\kappa := f/\kappa^2$. For $u_B \in V_B$ and $u_{B,S} \in V_{B,S_B}$, defined in (4.2) and (4.4), respectively, we have the estimates:

$$\|\kappa(u_B - u_{B,S})\|^2_{L^2(\Omega)} \leq \sum_{j=1}^{J} \frac{1}{|\lambda^j_* - 1|^2} \|\kappa(f_\kappa - P^j_{I_j} f_\kappa)\|^2_{L^2(\Omega_j)}, \tag{4.7}$$

$$\|\sqrt{a}\nabla(u_B - u_{B,S})\|^2_{L^2(\Omega)} \leq \sum_{j=1}^{J} \frac{\lambda^j_\#}{|\lambda^j_\# - 1|^2} \|\kappa(f_\kappa - P^j_{I_j} f_\kappa)\|^2_{L^2(\Omega_j)}, \tag{4.8}$$

where $\lambda^j_* = \operatorname{argmin}\{|\lambda^j_i - 1|, i \geq I_j + 1\}$, and $\lambda^j_\# = \operatorname{argmax}\left\{\frac{\lambda^j_i}{|\lambda^j_i - 1|^2}, i \geq I_j + 1\right\}$.

*Proof.* Since $\{b_i^j\}_i$ form an orthonormal basis for $L^2(\Omega_j)$ with the weighted inner product $(\kappa^2 u, v)_{\Omega_j}$, we may assume the expansion

$$u_B = \sum_{j=1}^{J} \sum_{i=1}^{\infty} u_{B,i}^j b_i^j, \qquad \text{with } u_{B,i}^j = (\kappa^2 u_B, b_i^j)_{\Omega_j}.$$

By testing equation (4.2) with $v_B = b_i^j$, for $i \in \mathbb{N}$, and observing that $\mathscr{C}(u_B, b_i^j) = \mathscr{A}_j(u_B, b_i^j) - (\kappa^2 u_B, b_i^j)_{\Omega_j}$, we infer from equation (3.2) that $u_{B,i}^j = F(b_i^j)/(\lambda_i^j - 1)$. Consequently, we obtain that

$$u_{B,S} = \sum_{j=1}^{J} \sum_{i=1}^{I_j} u_{B,S,i}^j b_i^j, \quad \text{with } u_{B,S,i}^j = \frac{F(b_i^j)}{\lambda_i^j - 1}.$$

Therefore, $u_{B,S,i}^j = u_{B,i}^j$ for $1 \le i \le I_j$ and $1 \le j \le J$. Since $b_i^j = 0$ on $\partial\Omega$, we further have that $F(b_i^j) = (f, b_i^j)_\Omega$. Hence, we conclude that

$$\|\kappa(u_B - u_{B,S})\|_{L^2(\Omega)}^2 = \sum_{j=1}^{J} \sum_{i=I_j+1}^{\infty} \frac{1}{|\lambda_i^j - 1|^2} |(f, b_i^j)_{\Omega_j}|^2,$$

which, by equation (4.6) and the definition of $\lambda_*^j$, implies (4.7). Estimate (4.8) follows similarly from $\mathscr{A}_j(b_i^j, b_i^j) = \lambda_i^j$ and

$$\|\sqrt{a}\nabla(u_B - u_{B,S})\|_{L^2(\Omega)}^2 = \sum_{j=1}^{J} \sum_{i=I_j+1}^{\infty} \frac{\lambda_i^j}{|\lambda_i^j - 1|^2} |(f, b_i^j)_{\Omega_j}|^2.$$

□

Remark 2. We note that, if $f_{|\Omega_j} = 0$, then $u_{B|\Omega_j} = 0$, and the approximation error vanishes on $\Omega_j$. Therefore, no bubble basis functions have to be computed on the corresponding domain $\Omega_j$. If, on the other hand, $f$ does not vanish on $\Omega_j$, the projection error in the estimates in Theorem 4.1 might be used to adaptively choose the number of required bubble functions that guarantee a certain error bound; cf. the discussion before (Hetmaniuk & Klawonn, 2014, Prop. 3.6) for the elliptic case.

Remark 3. From the proof of Theorem 4.1, we see that, per subdomain, the bubble approximation is a projection of the bubble part of the solution to Helmholtz equation with respect to the norms in (4.7) and (4.8). Since a projection constitutes the best-approximation and Assumption 3.1 can be interpreted as a resolution condition, the bubble approximation does not suffer from the pollution effect in the sense of Babuška & Sauter (1997).

### 4.2 *Well-posedness of the interface Galerkin problem*

Well-posedness of the Galerkin problem and quasi-best approximation results under an adjoint approximability condition follow as in (Graham & Sauter, 2019, Section 4), which has also been used in

(Chen *et al.*, 2023, Section 4.2) or (Ma *et al.*, 2023, Section 3.2) in a multiscale context. To state the result let us introduce $T^*\chi = z$, mapping $\chi \in L^2(\Omega)$ to the solution $z \in H^1_D(\Omega)$ of the dual problem

$$\mathscr{C}(v, z) = (v, \chi) \quad \text{for all } v \in H^1_D(\Omega), \tag{4.9}$$

which is well-defined due to Theorem 2.2. Moreover, we denote with $T^*_\Gamma \chi = E^\Gamma(z_{|\Gamma}) \in V_\Gamma$ the interface component of $T^*\chi$. Using equation (4.1), we observe that $T^*_\Gamma \chi$ is a solution to equation (4.9) for test functions $v \in V_\Gamma$. The approximation properties of the interface space $V_{\Gamma,S_\Gamma}$ are measured by the adjoint approximability constant

$$\sigma^* = \sup_{\varphi \in L^2(\Omega)\setminus\{0\}} \frac{\inf_{v_{\Gamma,S} \in V_{\Gamma,S_\Gamma}} \|T^*_\Gamma(\kappa^2\varphi) - v_{\Gamma,S}\|_{\mathscr{B}}}{\|\kappa\varphi\|_{L^2(\Omega)}}. \tag{4.10}$$

With these preparations, we can state the abstract result (Graham & Sauter, 2019, Thm. 4.2) in our setting.

Lemma 4.2. Suppose that $C_{\mathscr{C}}\sigma^* \leq 1/2$, where $C_{\mathscr{C}}$ is defined in equation (2.8) and $\sigma^*$ is the adjoint approximability constant. Then, the Galerkin problem (4.5) has a unique solution, and the following estimates hold:

$$\|u_\Gamma - u_{\Gamma,S}\|_{\mathscr{B}} \leq 2C_{\mathscr{C}} \inf_{v_{\Gamma,S} \in V_{\Gamma,S_\Gamma}} \|u_\Gamma - v_{\Gamma,S}\|_{\mathscr{B}}, \tag{4.11}$$

$$\|\kappa(u_\Gamma - u_{\Gamma,S})\|_{L^2(\Omega)} \leq 2C^2_{\mathscr{C}}\sigma^* \inf_{v_{\Gamma,S} \in V_{\Gamma,S_\Gamma}} \|u_\Gamma - v_{\Gamma,S}\|_{\mathscr{B}}. \tag{4.12}$$

Note that the quasi-optimality constant $2C_{\mathscr{C}}$ in (4.11) is independent of $\omega$ for large $\omega$; see Theorem 2.2. However, the result applies only if $\sigma^*$ is sufficiently small, which requires sufficiently many edge modes; see Section 4.4.

*Proof.* The proof follows closely Graham & Sauter (2019) and is included for convenience of the reader. Denote $e_\Gamma = u_\Gamma - u_{\Gamma,S}$, and let $\psi = T^*_\Gamma(\kappa^2 e_\Gamma)$. Then, for $\psi_{\Gamma,S} \in V_{\Gamma,S_\Gamma}$ being the best-approximation of $\psi$ in the $\mathscr{B}$-norm, Galerkin orthogonality yields

$$\|\kappa e_\Gamma\|^2_{L^2(\Omega)} = \mathscr{C}(e_\Gamma, \psi) = \mathscr{C}(e_\Gamma, \psi - \psi_{\Gamma,S}) \leq C_{\mathscr{C}}\sigma^*\|e_\Gamma\|_{\mathscr{B}}\|\kappa e_\Gamma\|_{L^2(\Omega)},$$

where we used (4.10) as follows:

$$\|\psi - \psi_{\Gamma,S}\|_{\mathscr{B}} = \inf_{v_{\Gamma,S} \in V_{\Gamma,S_\Gamma}} \|T^*_\Gamma(\kappa^2 e_\Gamma) - v_{\Gamma,S}\|_{\mathscr{B}} \leq \sigma^*\|\kappa e_\Gamma\|_{L^2(\Omega)}.$$

Using Galerkin orthogonality once again, we obtain for arbitrary $v_{\Gamma,S} \in V_{\Gamma,S_\Gamma}$ that

$$\begin{aligned}\|e_\Gamma\|^2_{\mathscr{B}} &= \Re\{\mathscr{C}(e_\Gamma, e_\Gamma)\} + 2\|\kappa e_\Gamma\|^2_{L^2(\Omega)} = \Re\{\mathscr{C}(e_\Gamma, u_\Gamma - v_{\Gamma,S})\} + 2\|\kappa e_\Gamma\|^2_{L^2(\Omega)} \\ &\leq C_{\mathscr{C}}\|e_\Gamma\|_{\mathscr{B}}\|u_\Gamma - v_{\Gamma,S}\|_{\mathscr{B}} + 2(C_{\mathscr{C}}\sigma^*)^2\|e_\Gamma\|^2_{\mathscr{B}}.\end{aligned}$$

The abstract error estimates (4.11) and (4.12) then follow using the assumption $\sigma^* \leq 1/(2C_{\mathscr{C}})$. Similarly, we can prove the existence of the Galerkin projection. Assume

$$\mathscr{C}(u_{\Gamma,S}, v_{\Gamma,S}) = 0 \quad \text{for all } v_{\Gamma,S} \in V_{\Gamma,S_\Gamma}.$$

We have to show that $u_{\Gamma,S} = 0$. As before, but using the previous identity and choosing $v_{\Gamma,S}$ as the best-approximation in the $\mathscr{B}$-norm of $T^*_\Gamma(\kappa^2 u_{\Gamma,S})$, we obtain

$$\|\kappa u_{\Gamma,S}\|^2_{L^2(\Omega)} = \mathscr{C}(u_{\Gamma,S}, T^*_\Gamma(\kappa^2 u_{\Gamma,S}) - v_{\Gamma,S}) \leq C_{\mathscr{C}}\sigma^* \|u_{\Gamma,S}\|_{\mathscr{B}} \|\kappa u_{\Gamma,S}\|_{L^2(\Omega)}.$$

Therefore, we have that

$$\|u_{\Gamma,S}\|^2_{\mathscr{B}} = \Re\{\mathscr{C}(u_{\Gamma,S}, u_{\Gamma,S})\} + 2\|\kappa u_{\Gamma,S}\|^2_{L^2(\Omega)} = 2\|\kappa u_{\Gamma,S}\|^2_{L^2(\Omega)} \leq 2(C_{\mathscr{C}}\sigma^*)^2 \|u_{\Gamma,S}\|^2_{\mathscr{B}},$$

which, by assumption $C_{\mathscr{C}}\sigma^* \leq 1/2$, yields that $u_{\Gamma,S} = 0$. □

### 4.3 *Estimates of the best-approximation error in $V_{\Gamma,S_\Gamma}$*

Quantitative estimates for the interface approximation error follow from localizing the error to single edges and applying the estimates proven in Lemma 3.4.

THEOREM 4.3. Suppose that $C_{\mathscr{C}}\sigma^* \leq 1/2$, where $C_{\mathscr{C}}$ is defined in (2.8) and $\sigma^*$ is the adjoint approximability constant. Moreover, assume that the solution $u$ to equation (2.3) satisfies $u \in H^2(e)$ for all $e \in \mathscr{E}$, and denote by $u_{\Gamma,S}$ the solution to equation (4.5). Then,

$$\|u_\Gamma - u_{\Gamma,S}\|_{\mathscr{B}} \leq \sum_{e\in\mathscr{E}} \frac{C}{(\lambda^e_{I_e+1})^{3/4}} \|\Delta_e u - P^e_{I_e}\Delta_e u\|_{L^2(e)}$$

for a constant $C > 0$, bounded by $O(\|\kappa\|_\infty)$, independent of $u$ and $u_{\Gamma,S}$.

*Proof.* According to Lemma 4.2, it suffices to estimate the best-approximation error $\inf_{v_{\Gamma,S}} \|u_\Gamma - v_{\Gamma,S}\|_{\mathscr{B}}$. By continuity of $u$, the nodal interpolant $I_\mathscr{V} u$ of $u$ is well-defined and, by construction, we obtain that $(u - I_\mathscr{V} u)_{|e} \in H^1_0(e)$. These observations motivate the choice

$$v_{\Gamma,S} = E^\Gamma I_\mathscr{V} u + \sum_{e\in\mathscr{E}} E^e P^e_{I_e}(u - I_\mathscr{V} u), \tag{4.13}$$

with $P^e_{I_e}$ introduced in equation (3.12). We then have that $u_\Gamma(p) - v_{\Gamma,S}(p) = 0$ for all $p \in \mathscr{V}$. Moreover, in view of Section 2.4, $(u_\Gamma - v_{\Gamma,S})_{|e} \in H^1_0(e) \subset H^{1/2}_{00}(e)$. Therefore, the error can be localized to single edges as follows:

$$u_{\Gamma|\Omega_j} - v_{\Gamma,S_{|\Omega_j}} = E^j(u_{|\partial\Omega_j} - v_{\Gamma,S_{|\partial\Omega_j}}) = \sum_{e\in\mathscr{E}, e\subset\partial\Omega_j} \left(E^e(u_{|e} - v_{\Gamma,S_{|e}})\right)_{|\Omega_j}. \tag{4.14}$$

From the latter identity and from the definition (2.7), we obtain the following estimate:

$$\begin{aligned}\|u_\Gamma - v_{\Gamma,S}\|_{\mathscr{B}}^2 &\le C\sum_j \sum_{e\in\mathscr{E},e\subset\partial\Omega_j} \|E^e(u_{|e} - v_{\Gamma,S_{|e}})_{|\Omega_j}\|_{\mathscr{B}}^2 \\ &\le (a_{\max} + \|\kappa\|_\infty^2) C \max_j (1 + 1/\beta^j)^2 \sum_{e\in\mathscr{E}} \|u - v_{\Gamma,S}\|_{H_{00}^{1/2}(e)}^2, \end{aligned} \tag{4.15}$$

where $C$ depends on the number of edges of a subdomain $\Omega_j$ and where we used (3.6) and equivalence of the $\mathscr{B}$-norm to the $H^1(\Omega_j)$-norm. The interpolation estimate (2.10) and Lemma 3.4 then yield the assertion. □

If the solution has more regularity, the convergence improves, as long as the derivatives of the edge modes do not grow too quickly, which is true, e.g., if $e$ is a line segment.

LEMMA 4.4. In addition to the assumptions of Theorem 4.3, suppose that $u \in H^3(e)$ for all $e \in \mathscr{E}$. Moreover, suppose that there is a constant $C > 0$ such that $|\partial_e \tau_i^e(p)| \le C\sqrt{\lambda_i^e}$ for all $i \in \mathbb{N}$ and $p \in \partial e$. Then there is a constant $C > 0$ such that

$$\|u_\Gamma - u_{\Gamma,S}\|_{\mathscr{B}} \le C \sum_{e\in\mathscr{E}} \frac{1}{\lambda_{I_e+1}^e} \|u\|_{H^3(e)}.$$

REMARK 4. According to the relation $\lambda_i^e \sim i^2$ stated in (3.10), Lemma 4.4 implies that the error will be dominated by $(\lambda_{I_e+1}^e)^{-1} \sim I_e^{-2}$. Hence, the error in the $\mathscr{B}$-norm will decrease quadratically in the number of edge mode functions.

*Proof.* In view of Theorem 4.3, it suffices to bound

$$\|\Delta_e u - P_{I_e}^e \Delta_e u\|_{L^2(e)} = \left(\sum_{i>I_e} |(\Delta_e u, \tau_i^e)_e|^2\right)^{1/2}.$$

Since $-\Delta_e \tau_i^e = \lambda_i^e \tau_i^e$ on $e$ by elliptic regularity, integration by parts yields that

$$\left(\Delta_e u, \tau_i^e\right)_e = -\frac{1}{\lambda_i^e}\left(\Delta_e u, \Delta_e \tau_i^e\right)_e = \frac{1}{\lambda_i^e}\left((\partial_e^3 u, \partial_e \tau_i^e)_e + \left[\Delta_e u \partial_e \tau_i^e\right]_q^p\right),$$

where $p, q$ denote the endpoints of $e$. Therefore, using the Cauchy–Schwarz inequality, the continuity of the embedding $H^1(e) \hookrightarrow C^0(\overline{e})$ (Adams, 1975, p. 97), we have that

$$|(\Delta_e u, \tau_i^e)_e| \le \frac{C}{\sqrt{\lambda_i^e}} \|u\|_{H^3(e)}.$$

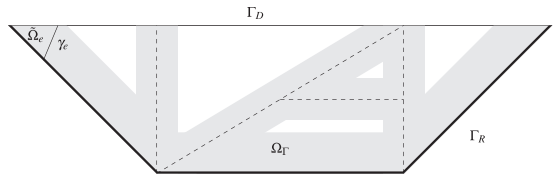


FIG. 1. A sketch of a polygonal domain $\Omega$ partitioned into 5 subdomains $\Omega_j, j = 1, \ldots, 5$. The portion $\Gamma_R$ is depicted in bold. The dashed lines and the edges in $\Gamma_R$ indicate the set of edges in $\mathscr{E}$. The light grey area corresponds to $\Omega_\Gamma$ defined in equation (4.16). The domain $\tilde{\Omega}_e$ with boundary portion $\gamma_e$ is used in Case 2 of the proof of Theorem 4.6.

Then, by using (3.10), we have that

$$\sum_{i>I_e} |(\Delta_e u, \tau_i^e)_e|^2 \leq C\|u\|^2_{H^3(e)} \sum_{i>I_e} \frac{1}{\lambda_i^e} \leq C \frac{\|u\|^2_{H^3(e)}}{\sqrt{\lambda^e_{I_e+1}}},$$

which proves the claim. □

REMARK 5. The error estimates in Theorem 4.3 and Lemma 4.4 assume regularity of the solution to the Helmholtz equation along the edges of the domain decomposition. By the trace theorem Grisvard (2011), this smoothness follows from regularity of the solution in a neighborhood of the edges, which can be established under suitable assumptions on the coefficients; see, e.g., (Gilbarg & Trudinger, 2001, Chapter 8), (Grisvard, 2011, Chapter 4) or (McLean, 2000, Chapter 4) and also Section 4.4. If the solution $u$ enjoys less regularity than required in the above statements, corresponding error estimates can still be proven. For instance, under the regularity $u \in W^{1,p}(\Omega)$, for $p > 2$, established above, the corresponding estimate to Theorem 4.3 will have the exponent $(p-2)/(4p) > 0$ instead of $3/4$. To derive the latter statement, we use that $H_0^{1-1/p}(e)$ is an interpolation space between $L^2(e)$ and $H_0^1(e)$ (Lions & Magenes, 1972, Ch. 1, Thm. 11.6), $H_{00}^{1/2}(e)$ is an interpolation space between $L^2(e)$ and $H_0^{1-1/p}(e)$ (Lions & Magenes, 1972, Ch. 1, Thm. 11.7), and that $(u - I_\gamma u)_{|e} \in W_0^{1-1/p,p}(e) \subset H_0^{1-1/p}(e) \subset H_{00}^{1/2}(e)$ can be approximated in $V^e$.

### 4.4 *Estimates for adjoint approximability constant*

The well-posedness and the error estimates for the interface problem in Section 4.2 relied on the smallness of the adjoint approximability constant $\sigma^*$ defined in equation (4.10). In order to estimate $\sigma^*$ in our setting, we follow the ideas of Graham & Sauter (2019), where they work with piecewise linear finite elements, requiring $H^2(\Omega)$-regularity of the adjoint problem (4.9). Since we need to consider the interface problem only, we can require a weaker $H^2$-regularity in the vicinity of the interface $\Gamma$. Let, for some fixed $\delta > 0$,

$$\Omega_\Gamma = \{x \in \Omega : \operatorname{dist}(x, \Gamma) < \delta\} \tag{4.16}$$

denote an open neighborhood of $\Gamma$, see Fig. 1. We start with a result similar to Theorem 4.3, but with slightly weaker regularity assumptions.

LEMMA 4.5. Let $\lambda^\Gamma = \min_e \lambda^e_{I_e}$. Then, there exists a constant $C > 0$ with $C = O(\|\kappa\|_\infty)$, such that, for all $z \in H^2(\Omega_\Gamma)$, it holds that

$$\inf_{v_{\Gamma,S} \in V_{\Gamma,S_\Gamma}} \|E^\Gamma(z_{|\Gamma}) - v_{\Gamma,S}\|_{\mathscr{B}} \leq \frac{C}{\sqrt{\lambda^\Gamma}} \|z\|_{H^2(\Omega_\Gamma)}. \tag{4.17}$$

*Proof.* In view of (4.15), which also introduces the $\kappa$ dependency of the constants, it suffices to estimate

$$\inf_{v^e \in V^e_{I_e}} \|z - I_{\mathscr{V}} z - v^e\|_{H^{1/2}_{00}(e)}$$

in terms of $\|z\|_{H^2(\Omega_\Gamma)}$. By embedding, $z \in H^2(\Omega_\Gamma)$ implies that $z \in H^{3/2}(e)$ for all $e \in \mathscr{E}$, and applying Lemma 3.5 yields that

$$\inf_{v_{\Gamma,S} \in V_{\Gamma,S_\Gamma}} \|z - v_{\Gamma,S}\|_{H^{1/2}_{00}(e)} \leq \frac{C}{\sqrt{\lambda^e_{I_e+1}}} \|z\|_{H^{3/2}(e)}.$$

Hence, the definition of $\lambda^\Gamma$ yields the assertion. □

Assuming regularity of the coefficients of the Helmholtz problem locally around the interface $\Gamma$, we can next estimate the adjoint approximability constant.

THEOREM 4.6. If $a \in C^{0,1}(\overline{\Omega_\Gamma})$ and $\beta \in C^{0,1}(\overline{\Gamma_R})$ are Lipschitz continuous functions, then there exists a constant $C > 0$ such that $C = O(\|\kappa\|^2_\infty C_{\text{stab}})$, with $C_{\text{stab}}$ from (2.9), and

$$\sigma^* \leq C/\sqrt{\lambda^\Gamma}. \tag{4.18}$$

*Proof.* In view of equation (4.10), the key for estimating $\sigma^*$ is to obtain an estimate for

$$\inf_{v_{\Gamma,S} \in V_{\Gamma,S_\Gamma}} \|T^*_\Gamma(\kappa^2 \varphi) - v_{\Gamma,S}\|_{\mathscr{B}}$$

in terms of $\|\kappa\varphi\|_{L^2(\Omega)}$ for arbitrary $\varphi \in L^2(\Omega)$, where $T^*_\Gamma(\kappa^2\varphi) \in V_\Gamma$ is the interface component of the solution to the adjoint problem (4.9). Using (4.17), we have the bound

$$\inf_{v_{\Gamma,S} \in V_{\Gamma,S_\Gamma}} \|T^*_\Gamma(\kappa^2 \varphi) - v_{\Gamma,S}\|_{\mathscr{B}} \leq \frac{C}{\sqrt{\lambda^\Gamma}} \|T^*(\kappa^2\varphi)\|_{H^2(\Omega_\Gamma)},$$

with $C = O(\|\kappa\|_\infty)$, provided $T^*(\kappa^2\varphi) \in H^2(\Omega_\Gamma)$. Next, we show that there exists a constant $C_* > 0$ such that $C_* = O(\|\kappa\|_\infty C_{\text{stab}})$, with $C_{\text{stab}}$ from (2.9), and

$$\|T^*(\kappa^2\varphi)\|_{H^2(\Omega_\Gamma)} \leq C_* \|\kappa\varphi\|_{L^2(\Omega)}, \tag{4.19}$$

which will conclude the proof.

We use the decomposition $\Omega_\Gamma = \cup_{e\in\mathscr{E}}\Omega_e$, with $\Omega_e = \{x \in \Omega : \mathrm{dist}(x, e) < \delta\}$ for $e \in \mathscr{E}$, and show an $H^2$-estimate for each $\Omega_e$. We observe that $z \in H^1_D(\Omega)$ is a weak solution to

$$-\mathrm{div}(a\nabla z) + z = \kappa^2\varphi + (\kappa^2 + 1)z =: \tilde{f} \quad \text{in } \Omega_e, \tag{4.20}$$

$$a\partial_n z = -i\beta\omega z =: \tilde{g} \quad \text{on } \partial\Omega_e \cap \Gamma_R, \tag{4.21}$$

$$z = 0 \quad \text{on } \partial\Omega_e \cap \Gamma_D, \tag{4.22}$$

with $\tilde{f} \in L^2(\Omega)$. We distinguish two cases; see also Fig. 1.

*Case 1:* suppose $\partial\Omega_e$ does not contain a vertex of $\partial\Omega$. In this case, either $\Omega_e \Subset \Omega$ or one of the boundary portions $\partial\Omega_e \cap \Gamma_D$, $\partial\Omega_e \cap \Gamma_R$ is not empty and of class $C^{1,1}$. Elliptic regularity, see, e.g., (McLean, 2000, Theorem 4.16, Theorem 4.18), ensures the existence of a constant $C > 0$, independent of $\kappa$, such that

$$\|z\|_{H^2(\Omega_e)} \le C\Big(\|z\|_{H^1(\Omega)} + \|\tilde{f}\|_{L^2(\Omega)} + \|\tilde{g}\|_{H^{1/2}(\partial\Omega_e\cap\Gamma_R)}\Big) \le C(1 + \|\kappa\|_\infty)(\|z\|_{\mathscr{B}} + \|\kappa\varphi\|_{L^2(\Omega)}), \tag{4.23}$$

where we used the trace theorem to bound $\|\tilde{g}\|_{H^{1/2}(\partial\Omega_e\cap\Gamma_R)}$ in terms of $\omega\|z\|_{H^1(\Omega_e)}$.

*Case 2:* if $\partial\Omega_e$ contains a vertex $s$ of $\partial\Omega$, we denote $B_\varepsilon$ the open ball with radius $\varepsilon$ around $s$. $H^2$-regularity of $z$ on $\Omega_e \setminus \overline{B_{\delta/2}}$ with an estimate corresponding to (4.23) then follows as in Case 1. Next, join the two segments contained in $B_{3\delta/4} \cap \partial\Omega$ by a smooth arc $\gamma_e \subset B_\delta$ such that the angles are smaller than $\pi/2$ and $s \notin \overline{\gamma_e}$. Denote the domain enclosed by $\gamma_e$ and $B_{3\delta/4} \cap \partial\Omega$ by $\tilde{\Omega}_e$. Thus, $z$ is also the unique weak solution to (4.20), (4.21), (4.22) with $\Omega_e$ replaced by $\tilde{\Omega}_e$, once we require the boundary condition $a\partial_n z = \tilde{g}_2$ on $\gamma_e$, with $\tilde{g}_2 := a\partial_n z$. Combining (Banasiak & Roach, 1989, Theorem 3.2.4) with the bounded inverse theorem and using the required conditions on the angles at the vertices of $\tilde{\Omega}_e$, we obtain that $z \in H^2(\tilde{\Omega}_e)$ and

$$\|z\|_{H^2(\tilde{\Omega}_e)} \le C\Big(\|\tilde{f}\|_{L^2(\tilde{\Omega}_e)} + \|\tilde{g}\|_{H^{1/2}_{pw}(\partial\tilde{\Omega}_e\cap\Gamma_R)} + \|\tilde{g}_2\|_{H^{1/2}(\gamma_e)}\Big),$$

where $\|\tilde{g}\|_{H^{1/2}_{pw}(\partial\tilde{\Omega}_e\cap\Gamma_R)}$ denotes the sum of $H^{1/2}$-norms over the corresponding segments of $\partial\tilde{\Omega}_e \cap \Gamma_R$. Combining the above estimates with (2.9) and the trace theorem to bound $\tilde{g}$ and $\tilde{g}_2$, we infer that

$$\|z\|_{H^2(\Omega_\Gamma)} \le C(1 + \|\kappa\|_\infty)C_{\mathrm{stab}}\|\kappa\varphi\|_{L^2(\Omega)},$$

with a constant $C$ independent of $\omega$. Hence, (4.19) holds with $C_* = C(1 + \|\kappa\|_\infty)C_{\mathrm{stab}}$. □

Since the method and its analysis presented here employ a fixed domain decomposition, the regularity assumption on the coefficients required in Theorem 4.6 might be verified in certain applications; see, e.g., the periodic structure in Section 5.4 below. A consequence of the previous result is that, by using sufficiently many edge modes, the assumptions of Lemma 4.2 can be verified. More precisely, if $C_{\mathrm{stab}}$ is independent of $\omega$, which holds in certain cases (Graham & Sauter, 2019, Theorem 4.5), we can use

TABLE 1 *Different errors in the $L^2$- (left) and $H^1$-norms (right) discussed in Section 5 row by row: absolute approximation errors of the ACMS solution $u_S$ with respect to the exact solution $u$, absolute approximation errors of the ACMS solution $u_S$ with respect to the finite element solution $u_{\text{FEM}}$, relative approximation errors of the ACMS solution $u_S$ with respect to the finite element solution $u_{\text{FEM}}$, approximation errors of the finite element solution $u_{\text{FEM}}$ with respect to the exact solution $u$ and interpolation error of the nodal interpolant $I_h(u)$ with respect to the exact solution $u$*

| $L^2$-errors | | $H^1$-errors | |
|---|---|---|---|
| $e_0$ | $\|u - u_S\|_{L^2(\Omega)}$ | $e_1$ | $\|u - u_S\|_{H^1(\Omega)}$ |
| $e_{0,h}$ | $\|u_{\text{FEM}} - u_S\|_{L^2(\Omega)}$ | $e_{1,h}$ | $\|u_{\text{FEM}} - u_S\|_{H^1(\Omega)}$ |
| $e^r_{0,h}$ | $e_{0,h}/\|u_{\text{FEM}}\|_{L^2(\Omega)}$ | $e^r_{1,h}$ | $e_{1,h}/\|u_{\text{FEM}}\|_{H^1(\Omega)}$ |
| $e_{0,\text{FEM}}$ | $\|u - u_{\text{FEM}}\|_{L^2(\Omega)}$ | $e_{1,\text{FEM}}$ | $\|u - u_{\text{FEM}}\|_{H^1(\Omega)}$ |
| $e_{0,\text{int}}$ | $\|u - I_h(u)\|_{L^2(\Omega)}$ | $e_{1,\text{int}}$ | $\|u - I_h(u)\|_{H^1(\Omega)}$ |

(3.10) and $\sigma^* = O(C_{\text{stab}}\|\kappa\|^2_\infty \max_e |e|/\min_e I_e)$ to infer that the number of modes should scale like $I_e \geq C\|\kappa\|^2_\infty |e|$ for stability. We obtain the following statement:

THEOREM 4.7. In addition to the assumptions of Theorem 4.3, 4.6 suppose that $u \in H^{2+\alpha}(e)$ for all $e \in \mathscr{E}$, for $\alpha = 0, 1$. Then, for some $C > 0$, and $\lambda^\Gamma$ sufficiently large, it holds

$$\|\kappa(u_\Gamma - u_{\Gamma,S})\|_{L^2(\Omega)} \leq \frac{C}{(\lambda^\Gamma)^{5/4+\alpha/4}} \sum_{e\in\mathscr{E}} \|u\|_{H^{2+\alpha}(e)}.$$

*Proof.* Inserting the estimate (4.18) for $\sigma^*$ and the error bounds stated in Theorem 4.3 (if $\alpha = 0$) or Lemma 4.4 (if $\alpha = 1$) into (4.12) yields the assertion. □

REMARK 6. Similarly to Remark 4, (3.10) implies that $(\lambda^e_{I_e+1})^{-3/2} \sim I_e^{-3}$. Hence, for $\alpha = 1$, the estimate in Theorem 4.7 implies that the error in the $L^2$-norm will decrease cubically in the number of edge mode functions.

## 5. Numerical results

We provide numerical experiments to support our theoretical results and show the effectiveness of our approach. Since, in general, we cannot compute the ACMS basis functions in equation (3.4), (3.13) analytically, we compute them approximately using an underlying finite element discretization that adopts piecewise linear and continuous functions. To do so, we employ a quasi-uniform triangulation of the computational domain $\Omega$ into (non-curved) triangles, such that each subdomain $\Omega_j$ is the union of elements of that triangulation; see, for instance, Fig. 2. We denote the corresponding finite element solution of the Helmholtz problem by $u_{\text{FEM}}$. Moreover, the resulting errors are quantified according to Table 1.

### 5.1 *Classical Helmholtz example*

Let $\Omega = B_1(0)$ be the unit disc and $\Gamma_R = \partial\Omega$. We first consider the boundary value problem given by equation (1.1), (1.2) with $a(x) = 1$, $\beta(x) = 1$. The source terms $f$ and $g$ are defined such that

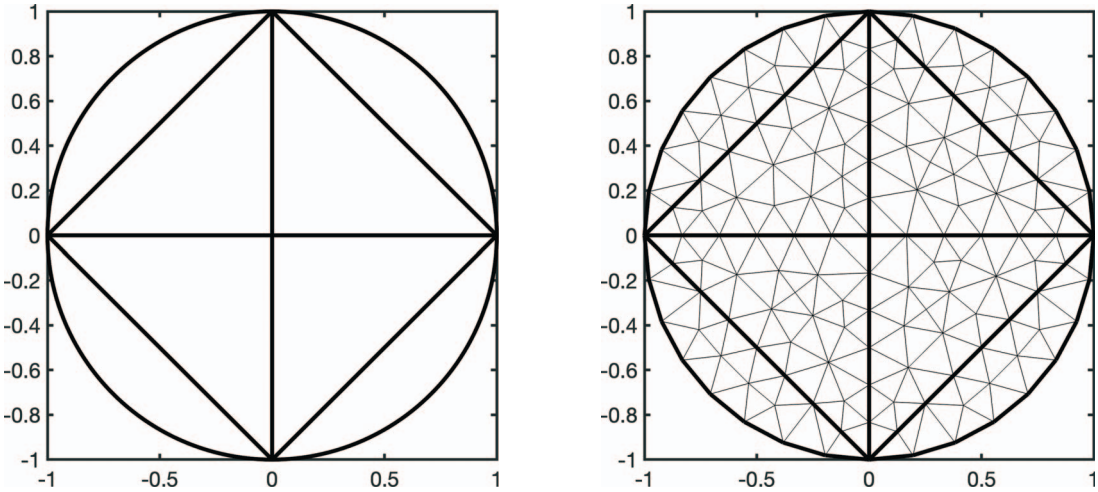


FIG. 2. **Left:** $\Omega$ is the unit disc, decomposed into eight subdomains. **Right:** The corresponding finite element mesh.

the problem has the plane wave solution $u(x) = \exp(-ik \cdot x)$, with wave vector $k = \kappa(0.6, 0.8)$ and variable wavenumber $\kappa = \omega$, i.e., $c(x) = 1$. In particular, $f(x) = 0$, therefore the solution satisfies $u_B = 0$, and $u$ can be approximated by solving the interface problem (4.5) only; see Theorem 4.1 and also Remark 2.

We employ a decomposition of $\Omega$ as depicted in Fig. 2 (left) with an initial coarse triangulation as shown in Fig. 2 (right), which corresponds to a domain decomposition into $J = 8$ subdomains. In this domain decomposition, the number of edges in $\mathscr{E}$ is 12 and the number of vertices in $\mathscr{V}$ equals 5. The ACMS solution $u_S$ and the finite element solution $u_{\text{FEM}}$ are computed using uniform refinements of the coarse triangulation; see Fig. 2 (right).

5.1.1 *Low wavenumber.* Let us first consider the case of a low wavenumber $\kappa = 1$. In this setting, we obtain $\|u\|_{H^1(\Omega)} \approx 2.5$ and $\|u\|_{L^2(\Omega)} \approx 1.8$ for the plane wave solution $u$. We compare the plane wave solution $u$ with the approximation $u_S$ given by the ACMS method for different underlying finite element discretizations and multi-indices $S_\Gamma$, which define the order of the interface approximation space $V_{\Gamma,S_\Gamma}$ introduced in equation (3.13). Moreover, we use the same value of $I_e \in \{2, 4, 8, \ldots, 64\}$ for each of the 12 edges in $\mathscr{E}$.

Table 2 shows the approximation error of the ACMS method and the corresponding errors for the nodal interpolant $I_h(u)$ for each mesh resolution. We observe that the $H^1$-error decreases quadratically, more precisely, by a factor between 3.5 and 4.0, until it approaches the accuracy of the nodal interpolant $I_h u$ of the underlying finite element mesh; see also Fig. 3. Similarly, the $L^2$-error decays cubically for sufficiently fine finite element meshes. The $L^2$-convergence is in good agreement with Theorem 4.7; see Remark 6; while the $H^1$-convergence is in good agreement with Lemma 4.4 and Remark 4 in this example. We may conclude that, already with a low number of edge modes $I_e \leq 32$, i.e., $|S_\Gamma| \leq 384$, the ACMS solution achieves the accuracy of the nodal interpolant in the $H^1$-norm, which employs around $8{\cdot}10^6$ vertices for $h \approx 3.4{\cdot}10^{-4}$. In fact, as shown in Table 3 and Fig. 4, the ACMS solution converges to the (standard) finite element solution $u_{\text{FEM}}$ quadratically in the $H^1$-norm and cubically in the $L^2$-norm, respectively.

TABLE 2 *Classical Helmholtz example with $\kappa = 1$: errors $e_0$ (top) and $e_1$ (bottom) as defined in Table 1 for different number of edge modes $|S_\Gamma| \in \{24, 48, \ldots, 768\}$, computed on different finite element meshes with mesh size h, and the corresponding interpolation error for the nodal interpolant*

| | | $\lvert S_\Gamma \rvert$ | | | | | |
|---|---|---|---|---|---|---|---|
| $h$ | $e_{0,\text{int}}$ | 24 | 48 | 96 | 192 | 384 | 768 |
| $1.3{\cdot}10^{-3}$ | $7.6{\cdot}10^{-7}$ | $4.2{\cdot}10^{-3}$ | $7.8{\cdot}10^{-4}$ | $1.2{\cdot}10^{-4}$ | $1.6{\cdot}10^{-5}$ | $2.6{\cdot}10^{-6}$ | $1.5{\cdot}10^{-6}$ |
| $6.9{\cdot}10^{-4}$ | $1.9{\cdot}10^{-7}$ | $4.2{\cdot}10^{-3}$ | $7.8{\cdot}10^{-4}$ | $1.2{\cdot}10^{-4}$ | $1.6{\cdot}10^{-5}$ | $2.2{\cdot}10^{-6}$ | $4.8{\cdot}10^{-7}$ |
| $3.4{\cdot}10^{-4}$ | $4.7{\cdot}10^{-8}$ | $4.2{\cdot}10^{-3}$ | $7.8{\cdot}10^{-4}$ | $1.2{\cdot}10^{-4}$ | $1.6{\cdot}10^{-5}$ | $2.1{\cdot}10^{-6}$ | $2.9{\cdot}10^{-7}$ |
| $h$ | $e_{1,\text{int}}$ | 24 | 48 | 96 | 192 | 384 | 768 |
| $1.3{\cdot}10^{-3}$ | $1.0{\cdot}10^{-3}$ | $5.8{\cdot}10^{-2}$ | $1.6{\cdot}10^{-2}$ | $4.6{\cdot}10^{-3}$ | $1.5{\cdot}10^{-3}$ | $1.1{\cdot}10^{-3}$ | $1.0{\cdot}10^{-3}$ |
| $6.9{\cdot}10^{-4}$ | $5.4{\cdot}10^{-4}$ | $5.8{\cdot}10^{-2}$ | $1.6{\cdot}10^{-2}$ | $4.5{\cdot}10^{-3}$ | $1.2{\cdot}10^{-3}$ | $6.1{\cdot}10^{-4}$ | $5.4{\cdot}10^{-4}$ |
| $3.4{\cdot}10^{-4}$ | $2.7{\cdot}10^{-4}$ | $5.8{\cdot}10^{-2}$ | $1.6{\cdot}10^{-2}$ | $4.4{\cdot}10^{-3}$ | $1.1{\cdot}10^{-3}$ | $4.0{\cdot}10^{-4}$ | $2.8{\cdot}10^{-4}$ |

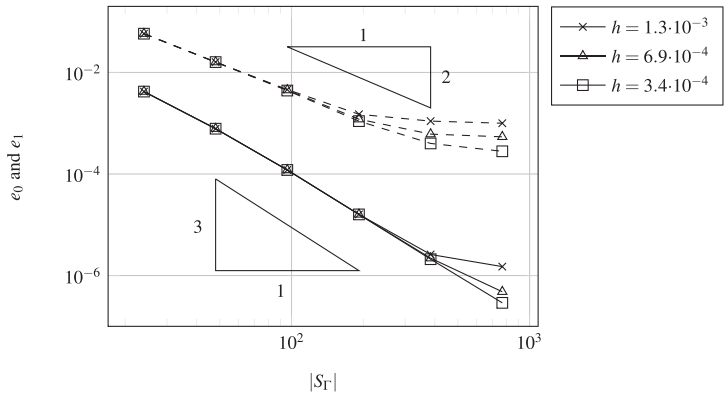


FIG. 3. Classical Helmholtz example with $\kappa = 1$: errors $e_0$ (solid) and $e_1$ (dashed) as presented in Table 2 on refined meshes of size $h$ for different number of edge modes $|S_\Gamma| \in \{24, 48, \ldots, 768\}$.

TABLE 3 *Classical Helmholtz example with $\kappa = 1$: errors $e_{0,h}$ and $e_{1,h}$ as defined in Table 1 for different number of edge modes $|S_\Gamma| \in \{24, 48, \ldots, 1536\}$, computed on a finite element mesh with $h \approx 3.4{\cdot}10^{-4}$ and 8 327 169 vertices*

| | $\lvert S_\Gamma \rvert$ | | | | | | |
|---|---|---|---|---|---|---|---|
| | 24 | 48 | 96 | 192 | 384 | 768 | 1536 |
| $e_{0,h}$ | $4.2{\cdot}10^{-3}$ | $7.8{\cdot}10^{-4}$ | $1.2{\cdot}10^{-4}$ | $1.6{\cdot}10^{-5}$ | $2.1{\cdot}10^{-6}$ | $2.7{\cdot}10^{-7}$ | $3.5{\cdot}10^{-8}$ |
| $e_{1,h}$ | $5.8{\cdot}10^{-2}$ | $1.6{\cdot}10^{-2}$ | $4.4{\cdot}10^{-3}$ | $1.1{\cdot}10^{-3}$ | $2.9{\cdot}10^{-4}$ | $7.4{\cdot}10^{-5}$ | $1.8{\cdot}10^{-5}$ |

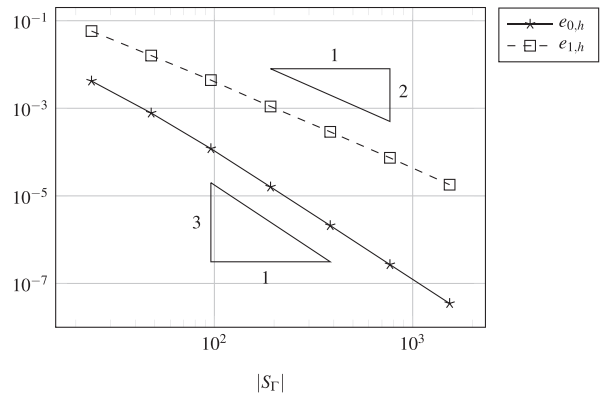


FIG. 4. Classical Helmholtz example with $\kappa = 1$: errors $e_{0,h}$ (solid) and $e_{1,h}$ (dashed) as shown in Table 3 for increasing number of edge modes $|S_\Gamma| \in \{24, 48, \ldots, 1536\}$ computed on a finite element mesh with $h \approx 3.4 \cdot 10^{-4}$.

5.1.2 *Higher wavenumbers.* We now repeat the previous numerical experiments focusing on the effect of an increasing wavenumber; namely, we test our method for $\kappa = 2, 4, 8, 16, 32, 64, 128$. Let us mention that Assumption 3.1 is satisfied for all chosen wavenumbers and that the plane wave solution $u$ changes with $\kappa$.

In Table 4 and Fig. 5, we show the convergence of the ACMS method to the plane wave solution and, for comparison, we display the error between the nodal interpolant and the finite element solution. For lower wavenumber $\kappa = 2$, we observe a similar behavior as in the previous section, i.e., close to cubic convergence of $e_0$ and close to quadratic convergence of $e_1$ until it occurs a saturation due to the limited resolution of the underlying FEM mesh.

For wavenumbers $\kappa \leq 64$, we observe that $e_{1,\text{int}}$ and $e_{1,\text{FEM}}$ behave very similarly when $\kappa$ is increased. However, if $\kappa = 128$, $e_{1,\text{FEM}}$ is more than one order of magnitude larger than $e_{1,\text{int}}$, which may indicate that the FEM mesh is too coarse for this wavenumber. For $|S_\Gamma| \geq 768$, i.e., at least 64 modes per edge, the ACMS error $e_1$ is close to the FEM error $e_{1,\text{FEM}}$ for all $\kappa$. We also observe that, for $\kappa \geq 32$, $|S_\Gamma|$ has to be sufficiently large to have monotonic decay in $e_1$. Notably, up to a certain number of edge modes, we may even see an increase in $e_1$. Ultimately, after reaching a certain threshold in the number of edge modes, which increases with $\kappa$, we observe a significant drop in the error $e_1$, bringing it to a comparable level as $e_{1,\text{FEM}}$.

The convergence of the ACMS solution to the FEM solution is also verified in Table 5 and Fig. 6, where the corresponding errors are shown for different wavenumbers. We observe a similar convergence behavior as for $e_1$ and $e_0$, respectively, without a saturation effect. If one is satisfied with the approximation errors achieved by $u_{\text{FEM}}$, we may again conclude that the ACMS method can yield good approximations already with a moderate number of degrees of freedom. We note that, by using higher order elements or further mesh refinements, the accuracy of $u_{\text{FEM}}$ may be increased; see, e.g., Melenk & Sauter (2010, 2011). Then, we would expect that the corresponding solution of the ACMS method would also show better accuracy in approximating the exact solution. We will investigate this in futurework.

## 5.2 *Localized interior source*

In certain applications, such as in geophysics in Wang *et al.* (2011), the source terms of the wave propagation are localized. Therefore, let us study the behavior of the ACMS method for this type of

TABLE 4 *Classical Helmholtz example with higher wavenumbers: errors $e_0$ (top) and $e_1$ (bottom) as defined in Table 1 for different number of edge modes $|S_\Gamma| \in \{48, 96, \ldots, 1536\}$ and wavenumbers $\kappa$, computed on a finite element mesh with $h \approx 3.4{\cdot}10^{-4}$ and 8 327 169 vertices. For comparison, we display the interpolation error for the nodal interpolant as well as the FEM approximation error $u_{\text{FEM}} - u$ in the $H^1$- and $L^2$-norm, respectively*

| | | | $\lvert S_\Gamma\rvert$ | | | | | |
|---|---|---|---|---|---|---|---|---|
| $\kappa$ | $e_{0,\text{int}}$ | $e_{0,\text{FEM}}$ | 48 | 96 | 192 | 384 | 768 | 1536 |
| 2 | $1.9{\cdot}10^{-7}$ | $4.4{\cdot}10^{-7}$ | $2.2{\cdot}10^{-3}$ | $3.6{\cdot}10^{-4}$ | $5.1{\cdot}10^{-5}$ | $6.8{\cdot}10^{-6}$ | $9.9{\cdot}10^{-7}$ | $4.5{\cdot}10^{-7}$ |
| 4 | $7.6{\cdot}10^{-7}$ | $3.5{\cdot}10^{-6}$ | $1.3{\cdot}10^{-2}$ | $1.6{\cdot}10^{-3}$ | $2.1{\cdot}10^{-4}$ | $2.7{\cdot}10^{-5}$ | $4.9{\cdot}10^{-6}$ | $4.5{\cdot}10^{-6}$ |
| 8 | $3.0{\cdot}10^{-6}$ | $4.2{\cdot}10^{-5}$ | $1.5{\cdot}10^{-1}$ | $7.8{\cdot}10^{-3}$ | $8.6{\cdot}10^{-4}$ | $1.1{\cdot}10^{-4}$ | $4.5{\cdot}10^{-5}$ | $4.2{\cdot}10^{-5}$ |
| 16 | $1.2{\cdot}10^{-5}$ | $4.2{\cdot}10^{-4}$ | $1.2{\cdot}10^{0}$ | $1.6{\cdot}10^{-1}$ | $6.0{\cdot}10^{-3}$ | $7.3{\cdot}10^{-4}$ | $4.3{\cdot}10^{-4}$ | $4.2{\cdot}10^{-4}$ |
| 32 | $4.8{\cdot}10^{-5}$ | $4.5{\cdot}10^{-3}$ | $4.9{\cdot}10^{0}$ | $2.2{\cdot}10^{0}$ | $3.5{\cdot}10^{-1}$ | $1.0{\cdot}10^{-2}$ | $4.7{\cdot}10^{-3}$ | $4.5{\cdot}10^{-3}$ |
| 64 | $1.9{\cdot}10^{-4}$ | $1.7{\cdot}10^{-2}$ | $2.4{\cdot}10^{0}$ | $2.0{\cdot}10^{0}$ | $2.7{\cdot}10^{0}$ | $8.7{\cdot}10^{-2}$ | $1.8{\cdot}10^{-2}$ | $1.7{\cdot}10^{-2}$ |
| 128 | $7.7{\cdot}10^{-4}$ | $4.3{\cdot}10^{-1}$ | $3.4{\cdot}10^{0}$ | $2.0{\cdot}10^{0}$ | $4.4{\cdot}10^{0}$ | $9.9{\cdot}10^{0}$ | $4.8{\cdot}10^{-1}$ | $4.3{\cdot}10^{-1}$ |
| $\kappa$ | $e_{1,\text{int}}$ | $e_{1,\text{FEM}}$ | 48 | 96 | 192 | 384 | 768 | 1536 |
| 2 | $1.0{\cdot}10^{-3}$ | $1.0{\cdot}10^{-3}$ | $4.8{\cdot}10^{-2}$ | $1.3{\cdot}10^{-2}$ | $3.7{\cdot}10^{-3}$ | $1.4{\cdot}10^{-3}$ | $1.1{\cdot}10^{-3}$ | $1.0{\cdot}10^{-3}$ |
| 4 | $4.3{\cdot}10^{-3}$ | $4.3{\cdot}10^{-3}$ | $2.2{\cdot}10^{-1}$ | $5.6{\cdot}10^{-2}$ | $1.4{\cdot}10^{-2}$ | $5.6{\cdot}10^{-3}$ | $4.4{\cdot}10^{-3}$ | $4.3{\cdot}10^{-3}$ |
| 8 | $1.7{\cdot}10^{-2}$ | $1.7{\cdot}10^{-2}$ | $1.8{\cdot}10^{0}$ | $2.3{\cdot}10^{-1}$ | $5.8{\cdot}10^{-2}$ | $2.2{\cdot}10^{-2}$ | $1.7{\cdot}10^{-2}$ | $1.7{\cdot}10^{-2}$ |
| 16 | $6.9{\cdot}10^{-2}$ | $6.9{\cdot}10^{-2}$ | $1.9{\cdot}10^{1}$ | $3.1{\cdot}10^{0}$ | $2.5{\cdot}10^{-1}$ | $8.9{\cdot}10^{-2}$ | $7.1{\cdot}10^{-2}$ | $6.9{\cdot}10^{-2}$ |
| 32 | $2.7{\cdot}10^{-1}$ | $3.1{\cdot}10^{-1}$ | $1.5{\cdot}10^{2}$ | $7.2{\cdot}10^{1}$ | $1.1{\cdot}10^{1}$ | $4.9{\cdot}10^{-1}$ | $3.2{\cdot}10^{-1}$ | $3.1{\cdot}10^{-1}$ |
| 64 | $1.1{\cdot}10^{0}$ | $1.5{\cdot}10^{0}$ | $1.5{\cdot}10^{2}$ | $1.3{\cdot}10^{2}$ | $1.7{\cdot}10^{2}$ | $6.1{\cdot}10^{0}$ | $1.6{\cdot}10^{0}$ | $1.5{\cdot}10^{0}$ |
| 128 | $4.4{\cdot}10^{0}$ | $5.5{\cdot}10^{1}$ | $4.3{\cdot}10^{2}$ | $2.5{\cdot}10^{2}$ | $5.7{\cdot}10^{2}$ | $1.2{\cdot}10^{3}$ | $6.2{\cdot}10^{1}$ | $5.5{\cdot}10^{1}$ |

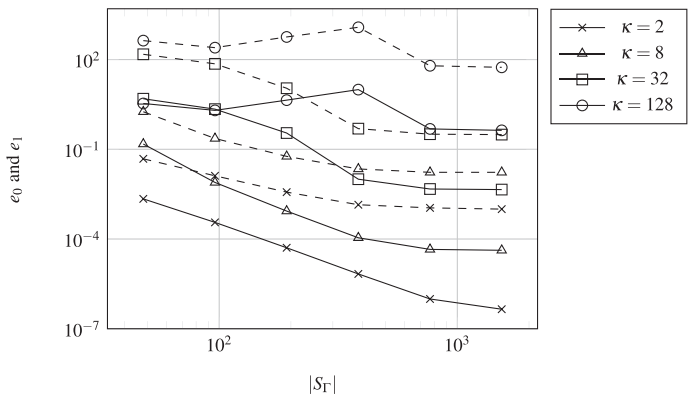


FIG. 5. Classical Helmholtz example with higher wavenumbers: errors $e_0$ (solid) and $e_1$ (dashed) as shown in Table 4 for increasing number of edge modes $|S_\Gamma| \in \{24, 48, \ldots, 1536\}$ for $h \approx 3.4{\cdot}10^{-4}$.

setup. Let us consider $\Omega = B_1(0)$ with $\Gamma_R = \partial\Omega$, the coefficients $a(x) = 1$ and $\beta(x) = 1$, the non-zero source function $f(x) = \exp(-200|x - x_c|^2)$, with $x_c = (1/3, 1/3)$, $\kappa = \omega = 1$, and $g \equiv 0$. For this example, no analytical expression of the solution $u$ is available. Thus, we only investigate the convergence of the

TABLE 5 *Classical Helmholtz example with higher wavenumbers: errors $e_{0,h}$ (top) and $e_{1,h}$ (bottom) as defined in Table 1 for different number of edge modes $|S_\Gamma| \in \{48, 96, \ldots, 1536\}$ and wavenumbers $\kappa$, computed on a finite element mesh with $h \approx 3.4{\cdot}10^{-4}$ and 8 327 169 vertices. For comparison, we display the interpolation error for the nodal interpolant as well as the FEM approximation error $u_{\text{FEM}} - u$ in the $H^1$- and $L^2$-norm, respectively*

| | | | $\lvert S_\Gamma\rvert$ | | | | | |
|---|---|---|---|---|---|---|---|---|
| $\kappa$ | $e_{0,\text{int}}$ | $e_{0,\text{FEM}}$ | 48 | 96 | 192 | 384 | 768 | 1536 |
| 2 | $1.9{\cdot}10^{-7}$ | $4.4{\cdot}10^{-7}$ | $2.2{\cdot}10^{-3}$ | $3.5{\cdot}10^{-4}$ | $4.9{\cdot}10^{-5}$ | $6.6{\cdot}10^{-6}$ | $8.5{\cdot}10^{-7}$ | $1.0{\cdot}10^{-7}$ |
| 4 | $7.6{\cdot}10^{-7}$ | $3.5{\cdot}10^{-6}$ | $1.3{\cdot}10^{-2}$ | $1.6{\cdot}10^{-3}$ | $2.1{\cdot}10^{-4}$ | $2.6{\cdot}10^{-5}$ | $3.3{\cdot}10^{-6}$ | $4.2{\cdot}10^{-7}$ |
| 8 | $3.0{\cdot}10^{-6}$ | $4.2{\cdot}10^{-5}$ | $1.5{\cdot}10^{-1}$ | $7.8{\cdot}10^{-3}$ | $8.5{\cdot}10^{-4}$ | $1.0{\cdot}10^{-4}$ | $1.3{\cdot}10^{-5}$ | $1.6{\cdot}10^{-6}$ |
| 16 | $1.2{\cdot}10^{-5}$ | $4.2{\cdot}10^{-4}$ | $1.2{\cdot}10^{0}$ | $1.6{\cdot}10^{-1}$ | $5.8{\cdot}10^{-3}$ | $5.0{\cdot}10^{-4}$ | $5.4{\cdot}10^{-5}$ | $6.6{\cdot}10^{-6}$ |
| 32 | $4.8{\cdot}10^{-5}$ | $4.5{\cdot}10^{-3}$ | $4.9{\cdot}10^{0}$ | $2.2{\cdot}10^{0}$ | $3.4{\cdot}10^{-1}$ | $7.2{\cdot}10^{-3}$ | $4.3{\cdot}10^{-4}$ | $3.4{\cdot}10^{-5}$ |
| 64 | $1.9{\cdot}10^{-4}$ | $1.7{\cdot}10^{-2}$ | $2.4{\cdot}10^{0}$ | $2.0{\cdot}10^{0}$ | $2.7{\cdot}10^{0}$ | $8.0{\cdot}10^{-2}$ | $2.2{\cdot}10^{-3}$ | $1.5{\cdot}10^{-4}$ |
| 128 | $7.7{\cdot}10^{-4}$ | $4.3{\cdot}10^{-1}$ | $3.4{\cdot}10^{0}$ | $2.0{\cdot}10^{0}$ | $4.5{\cdot}10^{0}$ | $9.9{\cdot}10^{0}$ | $2.4{\cdot}10^{-1}$ | $4.1{\cdot}10^{-3}$ |
| $\kappa$ | $e_{1,\text{int}}$ | $e_{1,\text{FEM}}$ | 48 | 96 | 192 | 384 | 768 | 1536 |
| 2 | $1.0{\cdot}10^{-3}$ | $1.0{\cdot}10^{-3}$ | $4.9{\cdot}10^{-2}$ | $1.3{\cdot}10^{-2}$ | $3.6{\cdot}10^{-3}$ | $9.4{\cdot}10^{-4}$ | $2.4{\cdot}10^{-4}$ | $6.0{\cdot}10^{-5}$ |
| 4 | $4.3{\cdot}10^{-3}$ | $4.3{\cdot}10^{-3}$ | $2.2{\cdot}10^{-1}$ | $5.6{\cdot}10^{-2}$ | $1.4{\cdot}10^{-2}$ | $3.6{\cdot}10^{-3}$ | $9.0{\cdot}10^{-4}$ | $2.2{\cdot}10^{-4}$ |
| 8 | $1.7{\cdot}10^{-2}$ | $1.7{\cdot}10^{-2}$ | $1.8{\cdot}10^{0}$ | $2.3{\cdot}10^{-1}$ | $5.6{\cdot}10^{-2}$ | $1.4{\cdot}10^{-2}$ | $3.5{\cdot}10^{-3}$ | $8.9{\cdot}10^{-4}$ |
| 16 | $6.9{\cdot}10^{-2}$ | $6.9{\cdot}10^{-2}$ | $1.9{\cdot}10^{1}$ | $3.0{\cdot}10^{0}$ | $2.4{\cdot}10^{-1}$ | $5.6{\cdot}10^{-2}$ | $1.4{\cdot}10^{-2}$ | $3.5{\cdot}10^{-3}$ |
| 32 | $2.7{\cdot}10^{-1}$ | $3.1{\cdot}10^{-1}$ | $1.5{\cdot}10^{2}$ | $7.2{\cdot}10^{1}$ | $1.1{\cdot}10^{1}$ | $3.4{\cdot}10^{-1}$ | $5.9{\cdot}10^{-2}$ | $1.4{\cdot}10^{-2}$ |
| 64 | $1.1{\cdot}10^{0}$ | $1.5{\cdot}10^{0}$ | $1.5{\cdot}10^{2}$ | $1.3{\cdot}10^{2}$ | $1.7{\cdot}10^{2}$ | $5.6{\cdot}10^{0}$ | $2.8{\cdot}10^{-1}$ | $5.8{\cdot}10^{-2}$ |
| 128 | $4.4{\cdot}10^{0}$ | $5.5{\cdot}10^{1}$ | $4.4{\cdot}10^{2}$ | $2.6{\cdot}10^{2}$ | $5.7{\cdot}10^{2}$ | $1.2{\cdot}10^{3}$ | $3.1{\cdot}10^{1}$ | $5.9{\cdot}10^{-1}$ |

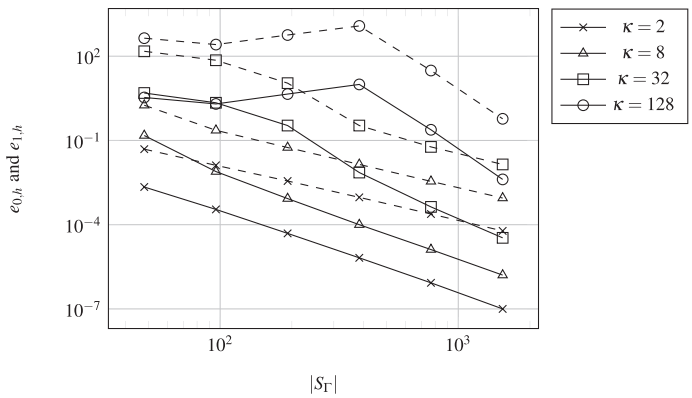


FIG. 6. Classical Helmholtz example with higher wavenumbers: errors $e_{0,h}$ (solid) and $e_{1,h}$ (dashed) as shown in Table 5 for increasing number of edge modes $|S_\Gamma| \in \{24, 48, \ldots, 1536\}$ for $h \approx 3.4{\cdot}10^{-4}$.

ACMS method towards the solution of the underlying FEM, which is justified by the discussion in the previous sections.

Table 6, Fig. 7, and Fig. 8 show the results for varying numbers of bubble functions and edge modes. In view of Theorem 4.1, we note that $u_B \approx 0$ outside the subdomain $\Omega_j$ with $x_c \in \Omega_j$. Hence, for

TABLE 6 *Example from Section* 5.2 *with a localized interior source. Relative errors* $e^r_{0,h}$ *(top) and* $e^r_{1,h}$ *(bottom) as defined in Table* 1 *for different number of edge modes* $|S_\Gamma| \in \{24, 48, \ldots, 1536\}$ *(in columns) and bubble functions* $|S_B|$ *(in rows) for* $h = 2.8{\cdot}10^{-3}$

| | $\lvert S_\Gamma\rvert$ | | | | | | |
|---|---|---|---|---|---|---|---|
| $\lvert S_B\rvert$ | 24 | 48 | 96 | 192 | 384 | 768 | 1536 |
| 2 | $5.4{\cdot}10^{-2}$ | $4.8{\cdot}10^{-2}$ | $4.7{\cdot}10^{-2}$ | $4.7{\cdot}10^{-2}$ | $4.7{\cdot}10^{-2}$ | $4.7{\cdot}10^{-2}$ | $4.7{\cdot}10^{-2}$ |
| 4 | $2.9{\cdot}10^{-2}$ | $2.6{\cdot}10^{-2}$ | $2.6{\cdot}10^{-2}$ | $2.6{\cdot}10^{-2}$ | $2.6{\cdot}10^{-2}$ | $2.6{\cdot}10^{-2}$ | $2.6{\cdot}10^{-2}$ |
| 8 | $2.5{\cdot}10^{-2}$ | $1.7{\cdot}10^{-2}$ | $1.7{\cdot}10^{-2}$ | $1.7{\cdot}10^{-2}$ | $1.7{\cdot}10^{-2}$ | $1.7{\cdot}10^{-2}$ | $1.7{\cdot}10^{-2}$ |
| 16 | $2.1{\cdot}10^{-2}$ | $9.9{\cdot}10^{-3}$ | $9.5{\cdot}10^{-3}$ | $9.5{\cdot}10^{-3}$ | $9.5{\cdot}10^{-3}$ | $9.5{\cdot}10^{-3}$ | $9.5{\cdot}10^{-3}$ |
| 32 | $1.9{\cdot}10^{-2}$ | $4.4{\cdot}10^{-3}$ | $3.2{\cdot}10^{-3}$ | $3.2{\cdot}10^{-3}$ | $3.2{\cdot}10^{-3}$ | $3.2{\cdot}10^{-3}$ | $3.2{\cdot}10^{-3}$ |
| 64 | $1.9{\cdot}10^{-2}$ | $2.8{\cdot}10^{-3}$ | $6.2{\cdot}10^{-4}$ | $6.1{\cdot}10^{-4}$ | $6.1{\cdot}10^{-4}$ | $6.1{\cdot}10^{-4}$ | $6.1{\cdot}10^{-4}$ |
| 128 | $1.9{\cdot}10^{-2}$ | $2.8{\cdot}10^{-3}$ | $1.5{\cdot}10^{-4}$ | $4.3{\cdot}10^{-5}$ | $4.2{\cdot}10^{-5}$ | $4.2{\cdot}10^{-5}$ | $4.2{\cdot}10^{-5}$ |
| 256 | $1.9{\cdot}10^{-2}$ | $2.8{\cdot}10^{-3}$ | $1.4{\cdot}10^{-4}$ | $1.0{\cdot}10^{-5}$ | $1.4{\cdot}10^{-6}$ | $3.6{\cdot}10^{-7}$ | $3.1{\cdot}10^{-7}$ |
| 512 | $1.9{\cdot}10^{-2}$ | $2.8{\cdot}10^{-3}$ | $1.4{\cdot}10^{-4}$ | $1.0{\cdot}10^{-5}$ | $1.4{\cdot}10^{-6}$ | $1.8{\cdot}10^{-7}$ | $4.1{\cdot}10^{-8}$ |
| 1024 | $1.9{\cdot}10^{-2}$ | $2.8{\cdot}10^{-3}$ | $1.4{\cdot}10^{-4}$ | $1.0{\cdot}10^{-5}$ | $1.4{\cdot}10^{-6}$ | $1.8{\cdot}10^{-7}$ | $3.1{\cdot}10^{-8}$ |
| $\lvert S_B\rvert$ | 24 | 48 | 96 | 192 | 384 | 768 | 1536 |
| 2 | $3.6{\cdot}10^{-1}$ | $3.4{\cdot}10^{-1}$ | $3.4{\cdot}10^{-1}$ | $3.4{\cdot}10^{-1}$ | $3.4{\cdot}10^{-1}$ | $3.4{\cdot}10^{-1}$ | $3.4{\cdot}10^{-1}$ |
| 4 | $2.6{\cdot}10^{-1}$ | $2.4{\cdot}10^{-1}$ | $2.4{\cdot}10^{-1}$ | $2.4{\cdot}10^{-1}$ | $2.4{\cdot}10^{-1}$ | $2.4{\cdot}10^{-1}$ | $2.4{\cdot}10^{-1}$ |
| 8 | $2.1{\cdot}10^{-1}$ | $1.9{\cdot}10^{-1}$ | $1.8{\cdot}10^{-1}$ | $1.8{\cdot}10^{-1}$ | $1.8{\cdot}10^{-1}$ | $1.8{\cdot}10^{-1}$ | $1.8{\cdot}10^{-1}$ |
| 16 | $1.6{\cdot}10^{-1}$ | $1.2{\cdot}10^{-1}$ | $1.2{\cdot}10^{-1}$ | $1.2{\cdot}10^{-1}$ | $1.2{\cdot}10^{-1}$ | $1.2{\cdot}10^{-1}$ | $1.2{\cdot}10^{-1}$ |
| 32 | $1.1{\cdot}10^{-1}$ | $5.9{\cdot}10^{-2}$ | $5.4{\cdot}10^{-2}$ | $5.4{\cdot}10^{-2}$ | $5.4{\cdot}10^{-2}$ | $5.4{\cdot}10^{-2}$ | $5.4{\cdot}10^{-2}$ |
| 64 | $1.0{\cdot}10^{-1}$ | $2.7{\cdot}10^{-2}$ | $1.3{\cdot}10^{-2}$ | $1.3{\cdot}10^{-2}$ | $1.3{\cdot}10^{-2}$ | $1.3{\cdot}10^{-2}$ | $1.3{\cdot}10^{-2}$ |
| 128 | $1.0{\cdot}10^{-1}$ | $2.3{\cdot}10^{-2}$ | $2.5{\cdot}10^{-3}$ | $1.2{\cdot}10^{-3}$ | $1.2{\cdot}10^{-3}$ | $1.2{\cdot}10^{-3}$ | $1.2{\cdot}10^{-3}$ |
| 256 | $1.0{\cdot}10^{-1}$ | $2.3{\cdot}10^{-2}$ | $2.1{\cdot}10^{-3}$ | $3.5{\cdot}10^{-4}$ | $9.2{\cdot}10^{-5}$ | $2.7{\cdot}10^{-5}$ | $1.5{\cdot}10^{-5}$ |
| 512 | $1.0{\cdot}10^{-1}$ | $2.3{\cdot}10^{-2}$ | $2.1{\cdot}10^{-3}$ | $3.5{\cdot}10^{-4}$ | $9.1{\cdot}10^{-5}$ | $2.4{\cdot}10^{-5}$ | $8.0{\cdot}10^{-6}$ |
| 1024 | $1.0{\cdot}10^{-1}$ | $2.3{\cdot}10^{-2}$ | $2.1{\cdot}10^{-3}$ | $3.5{\cdot}10^{-4}$ | $9.1{\cdot}10^{-5}$ | $2.4{\cdot}10^{-5}$ | $7.8{\cdot}10^{-6}$ |

an accurate approximation, we only need bubble functions in that subdomain $\Omega_j$. Moreover, the linear system for the bubble component is diagonal and decoupled from the interface part. Consequently, the solution coefficient corresponding to a specific bubble basis function can be computed independently from any other ACMS basis function; cf. equations (4.4) and (4.5).

For this highly localized source, in Fig. 8, we observe very fast convergence to the finite element solution when $I_j \geq 32$, i.e., when increasing the number of bubble functions, given a sufficiently high number of edge modes. This can be explained by inspecting the proof of Theorem 4.1: using repeatedly equation (3.2), integration-by-parts and that $f$ and all its derivative are negligible on $\partial\Omega_j$, we can estimate $(f, b_i^j)_{\Omega_j}$ by arbitrary powers of $\lambda_i^j$; see also Lemma 4.4 for similar steps. For a high number of bubble functions, a saturation effect occurs. This can be due to the limited quantity of edge modes or to the fact that the values of higher-order derivatives of $f$ are not negligible anymore. In Fig. 7, we see that when increasing the number of selected edge modes while keeping the number of bubble functions fixed, the convergence approaches the predicted quadratic and cubic rates for the $H^1$- and the $L^2$-error, respectively. Since the Galerkin problems for the bubble part and the interface are decoupled (see (4.4) and (4.5)), the

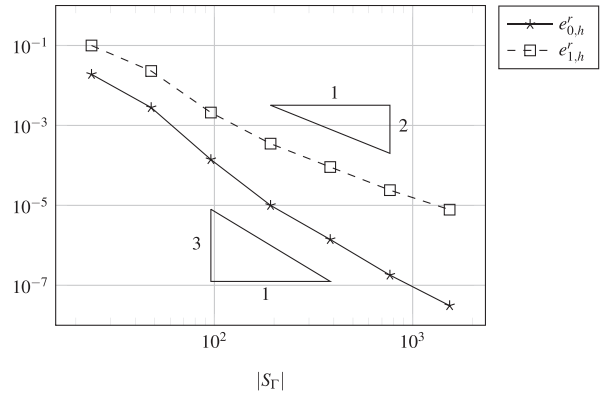


FIG. 7. Example from Section 5.2 with a localized interior source. Relative errors $e^r_{0,h}$ (solid) and $e^r_{1,h}$ (dashed) as shown in Table 6 for varying number of edge modes $|S_\Gamma| \in \{24, 48, \ldots, 1536\}$, fixed number of bubble modes $|S_B| = 1024$ and $h = 2.8{\cdot}10^{-3}$.

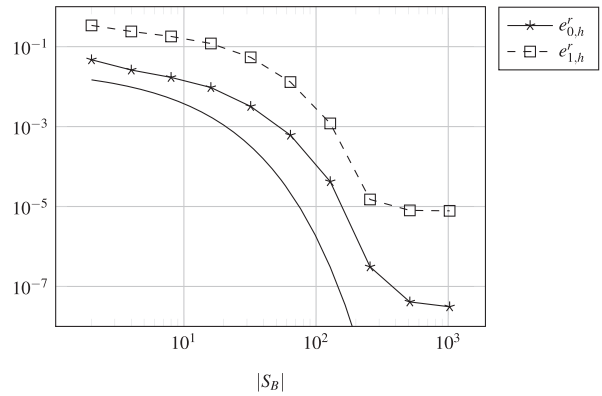


FIG. 8. Example from Section 5.2 with a localized interior source. Relative errors $e^r_{0,h}$ (solid) and $e^r_{1,h}$ (dashed) as shown in Table 6 for varying number of bubble functions $|S_B| = \{2, ..., 1024\}$, fixed number of edge modes $|S_\Gamma| = 1536$ and $h = 2.8 \cdot 10^{-3}$. For comparison, we show the exponential curve $0.06\exp(-0.28x^{0.67})$.

size of the systems to be solved remains comparably small. Therefore, we conclude that, for a moderate number of degrees of freedom, we obtain very good approximations of the finite element solution.

### 5.3 *Localized boundary source*

Let us modify the classical Helmholtz example from Section 5.1 such that $\kappa = \omega = 16, f = 0$ and $g(x) = \exp(-200|x - x_c|^2)$, with $x_c = (-1/\sqrt{2}, 1/\sqrt{2})$. In Fig. 9, we display the real and imaginary part of the finite element solution computed on a quasi-uniform mesh with 521 217 vertices, i.e., $h \approx 1.3 \cdot 10^{-3}$. Although the source is very localized around $x_c$, the whole domain is excited, indicating the wave-type behavior of the solution.

Since $f = 0$ here, we do not need any bubble functions to obtain convergence according to Remark 2. As we do not have an analytic solution, we investigate the error between $u_{\text{FEM}}$ and $u_S$ for varying number of edge modes. The results are shown in Table 7 and Fig. 10, where we consider the relative

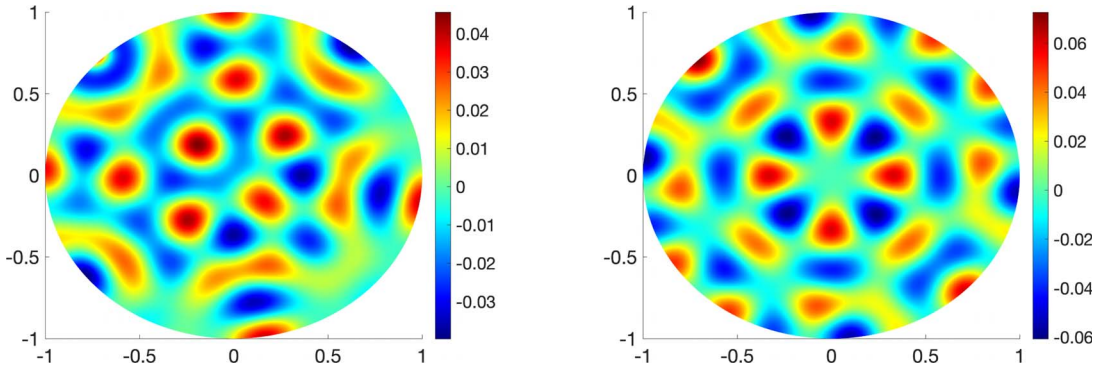


FIG. 9. Finite element solution of the model problem with a localized boundary source from Section 5.3: real part (left) and imaginary part (right).

TABLE 7 *Example from Section* 5.4 *with a localized boundary source: relative errors* $e^r_{0,h}$ *and* $e^r_{1,h}$ *as defined in Table* 1 *for different number of edge modes* $|S_\Gamma| \in \{24, 48, \ldots, 3072\}$*, computed on a grid with* $h = 1.3{\cdot}10^{-3}$

| | $\lvert S_\Gamma \rvert$ | | | | | | | |
|---|---|---|---|---|---|---|---|---|
| | 24 | 48 | 96 | 192 | 384 | 768 | 1536 | 3072 |
| $e^r_{0,h}$ | $1.6{\cdot}10^{0}$ | $1.0{\cdot}10^{0}$ | $1.7{\cdot}10^{-1}$ | $7.3{\cdot}10^{-3}$ | $4.1{\cdot}10^{-4}$ | $3.3{\cdot}10^{-5}$ | $3.5{\cdot}10^{-6}$ | $4.3{\cdot}10^{-7}$ |
| $e^r_{1,h}$ | $1.6{\cdot}10^{0}$ | $1.0{\cdot}10^{0}$ | $1.8{\cdot}10^{-1}$ | $1.4{\cdot}10^{-2}$ | $1.9{\cdot}10^{-3}$ | $4.6{\cdot}10^{-4}$ | $1.1{\cdot}10^{-4}$ | $2.8{\cdot}10^{-5}$ |

errors since the solution values are rather small. As predicted by Theorem 4.3, we observe second order convergence for the $H^1$-error, while the decay is initially slightly faster. The $L^2$-error shows a similar behavior with a convergence rate approaching third order; cf. Theorem 4.7. We again may conclude that we can approximate the highly resolved standard finite element solution using a moderate number of edge modes in the ACMS method.

### 5.4 *Periodic structure*

Let us conclude our numerical experiments with a heterogeneous Helmholtz problem on the unit square $\Omega = [0,1]^2$ with a domain decomposition as in Fig. 11 (left) and with a heterogeneous diffusion coefficient $a$ depicted in Fig. 11 (right). This configuration is similar to the modeling of two-dimensional photonic crystals in Joannopoulos *et al.* (2008). We choose $\beta(x) = 1$, interior source $f = 0$, and the localized boundary source on $\Gamma_R = \partial\Omega$, $g(x) = \exp(-ik \cdot x)\exp(-100|x - x_c|^2)$, with $x_c = (0, 1/2)$, wave vector $k = \kappa(1, 0)$ and wavenumber $\kappa = \omega = 100$. The corresponding finite element solution, which has been computed on a quasi-uniform triangulation with 5 330 337 vertices, is shown in Fig. 12.

Since, again, $f = 0$, we only need to study the behavior for varying numbers of edge modes, while the bubble part of the solution $u_B$ is zero. Note that we can choose $\Omega_\Gamma$ defined in equation (4.16) inside the region with $a = 1$; cf. Fig. 11. The relative $H^1$- and $L^2$-errors between the finite element solution and the ACMS solution are listed in Table 8 and shown in Fig. 13. For $|S_\Gamma| = 2880$, which corresponds to the case of 16 modes per edge, the ACMS discretization already yields a good approximation to the

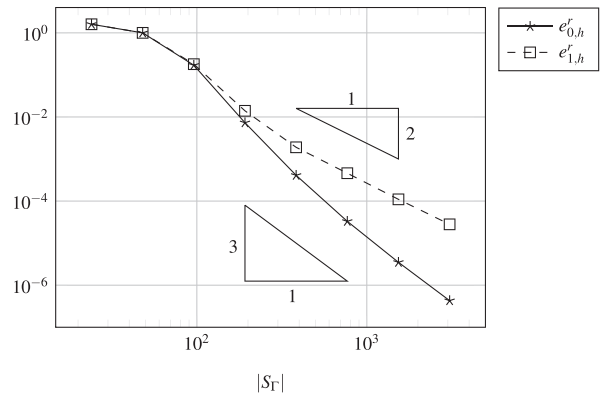


FIG. 10. Example 5.4: Localized boundary source: relative errors $e^r_{0,h}$ (solid) and $e^r_{1,h}$ (dashed) as shown in Table 7 for increasing number of edge modes $|S_\Gamma| \in \{24, 48, \ldots, 3072\}$, with $h = 1.3{\cdot}10^{-3}$.

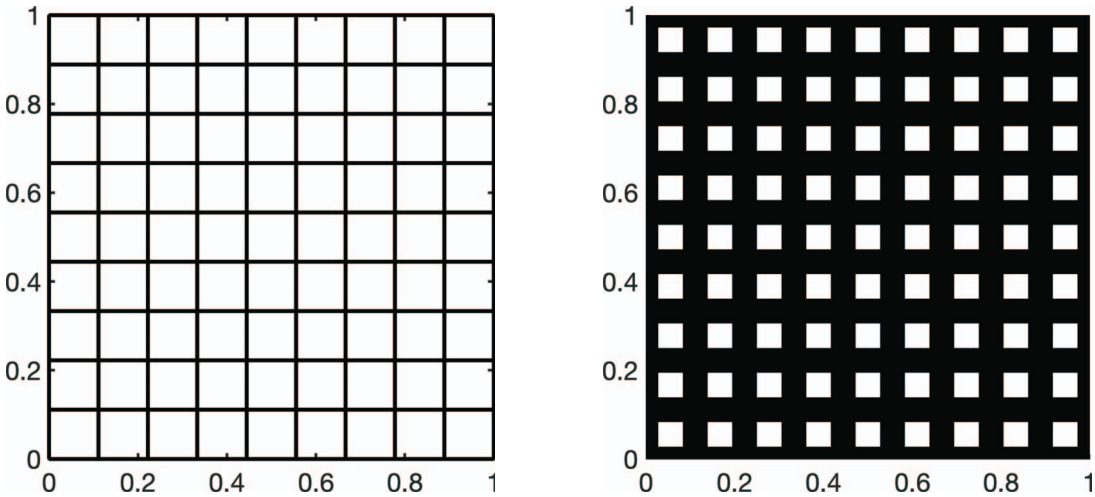


FIG. 11. **Left:** unit square divided in 81 subdomains for domain decomposition. The number of edges in $\mathscr{E}$ is 180 and the number of vertices in $\mathscr{V}$ is 100. **Right:** heterogeneous diffusion coefficient with $a = 1$ in the black regions and $a = 12$ in the white regions of the unit square.

TABLE 8 *Example from Section* 5.4*: periodic structure. Relative errors* $e^r_{0,h}$ *and* $e^r_{1,h}$ *as defined in Table* 1 *for different number of edge modes* $|S_\Gamma|$ *computed on a grid with* 5 330 337 *vertices.*

| | $\lvert S_\Gamma\rvert$ | | | | | |
|---|---|---|---|---|---|---|
| | 360 | 720 | 1 440 | 2 880 | 5 760 | 11 520 |
| $e^r_{0,h}$ | $1.1{\cdot}10^{0}$ | $1.3{\cdot}10^{0}$ | $1.6{\cdot}10^{-1}$ | $1.0{\cdot}10^{-2}$ | $7.5{\cdot}10^{-4}$ | $5.0{\cdot}10^{-5}$ |
| $e^r_{1,h}$ | $1.1{\cdot}10^{0}$ | $1.3{\cdot}10^{0}$ | $1.7{\cdot}10^{-1}$ | $1.1{\cdot}10^{-2}$ | $1.3{\cdot}10^{-3}$ | $2.9{\cdot}10^{-4}$ |

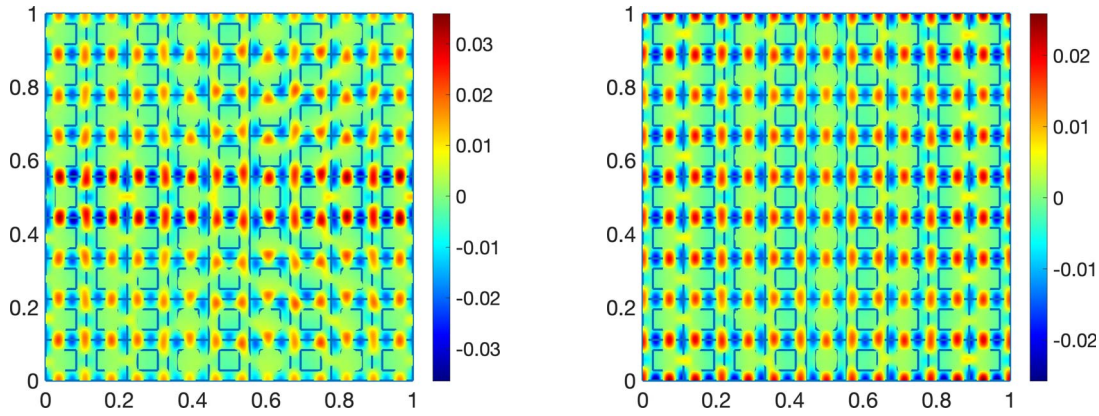


FIG. 12. Finite element solution of the model problem with a localized boundary source from Section 5.4: real part (left) and imaginary part (right); the underlying structure of the coefficient $a$ is shown as well

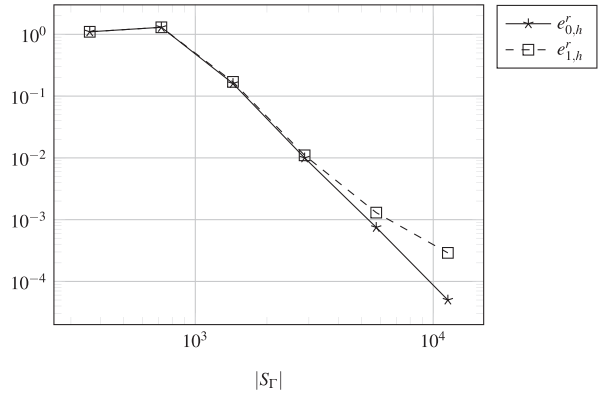


FIG. 13. Example 5.4: Periodic structure. Relative errors $e^r_{0,h}$ (solid) and $e^r_{1,h}$ (dashed) as shown in Table 8 for different number of edge modes $|S_\Gamma|$ computed on a grid with 5 330 337 vertices.

highly resolved finite element solution. Moreover, the convergence of the error is initially even better than predicted by our theoretical results for $|S_\Gamma| \geq 720$.

## 6. Conclusions

We extended the ACMS method, which has originally been developed for elliptic problems, to the heterogeneous Helmholtz equation. This framework is based on a decomposition into local Helmholtz problems and an interface problem, that can be solved separately. The numerical approximation of those problems is achieved by using basis functions with local support and which can be constructed locally as well. We note that the method presented here can also be applied to elliptic problems. Since the asymptotic behavior of the edge-eigenvalues (3.10) is available, we obtain explicit error bounds in terms of the number of edge modes.

The error analysis developed for the investigated method is based on the abstract framework introduced in Graham & Sauter (2019). We proved error estimates in the $H^1$- and the $L^2$-norm, and we obtained algebraic decay in the number of basis functions (modes) being used.

Asymptotically, these rates are worse than the $\mathcal{O}(H\exp(-I_e^{1/(d+1)-\varepsilon}))$ presented in Chen *et al.* (2023). For moderate number of modes $I_e$, however, the cubic and quadratic curves are below the exponential curve (assuming similar constants). A proper comparison of the two methods, including a quantification of the hidden constants in the error estimates, in applications relevant scenarios, is left for future work.

In order to be able to apply the framework of Graham & Sauter (2019), we presented estimates for the adjoint approximability constants, showing that the number of edgemodes should scale essentially like $C_{\text{stab}}(\omega)\|\kappa\|_\infty^2|e|/I_e$. Thus, if $C_{\text{stab}}(\omega)$ depends only weakly on $\omega$, the required number of edgemodes is moderate. If, however, $C_{\text{stab}}(\omega)$ grows quickly, it might be necessary to resort to other methods, such as Peterseim (2017), Chen *et al.* (2023) and Ma *et al.* (2023). Moreover, we showed applicability of the method also if the diffusion coefficient is not smooth, as long as smoothness in a neighborhood of the interface is guaranteed.

Finally, we exemplified the theoretical error bounds by numerical experiments, which show the accuracy of the inspected ACMS method for moderate wavenumbers. We constructed the ACMS basis functions using an FEM, and we observed that the resulting discrete ACMS method approximates well the corresponding finite element solution. Thus, we may conclude that the accuracy of the discrete ACMS method depends on the accuracy of the underlying FEM, and smaller errors might be achieved by using high-order finite elements.

## Acknowledgments

The authors thank Paula Kuhn and Jascha Knepper (Department of Mathematics and Computer Science, University of Cologne) for their insightful comments and the discussions on the draft of the manuscript.

## Funding

4TU.AMI SRI *Bridging Numerical Analysis and Machine Learning* (to A.H. and M.S.); Dutch Research council (NWO) (grant OCENW.GROOT.2019.071 to E.G. and M.S.

## Data availability

The data underlying this article are available in Zenodo, at https://dx.doi.org/10.5281/zenodo.8398791 Giammatteo *et al.* (2023).

## References

Aarnes, J. & Hou, T. Y. (2002) Multiscale domain decomposition methods for elliptic problems with high aspect ratios. *Acta Math. Appl. Sin. English Series.*, **18**, 63–76.

Abdulle, A., E., B. & Vanden-Eijnden, E. (2012) The heterogeneous multiscale method. *Acta Numer.*, **21**, 1–87.

Abdulle, A., Weinan, E. & Engquist, B. (2003) The heterogeneous multiscale methods. *Commun. Math. Sci.*, **1**, 87–132.

Adams, R. A. (1975) *Sobolev Spaces. Pure and Applied Mathematics*. New York, San Francisco, London: Academic Press.

Altmann, R., Henning, P. & Peterseim, D. (2021) Numerical homogenization beyond scale separation. *Acta Numer.*, **30**, 1–86. Publisher: Cambridge University Press.

Babuška, I., Banerjee, U. & Osborn, J. E. (2004) Generalized finite element methods — main ideas, results and perspective. *Int. J. Comput. Methods*, **01**, 67–103. Publisher: World Scientific Publishing Co.

Babuška, I., Caloz, G. & Osborn, J. E. (1994) Special finite element methods for a class of second order elliptic problems with rough coefficients. *SIAM J. Numer. Anal.*, **31**, 945–981.

Babuška, I., Ihlenburg, F., Paik, E. T. & Sauter, S. A. (1995) A generalized finite element method for solving the Helmholtz equation in two dimensions with minimal pollution. *Comput. Methods Appl. Mech. Eng.*, **128**, 325–359.

Babuška, I. & Osborn, J. E. (1983) Generalized finite element methods: Their performance and their relation to mixed methods. *SIAM J. Numer. Anal.*, **20**, 510–536.

Babuška, I. M. & Sauter, S. A. (1997) Is the pollution effect of the FEM avoidable for the Helmholtz equation considering high wave numbers? *SIAM J. Numer. Anal.*, **34**, 2392–2423.

Banasiak, J. & Roach, G. F. (1989) On mixed boundary value problems of Dirichlet oblique-derivative type in plane domains with piecewise differentiable boundary. *J. Differ. Equ.*, **79**, 111–131.

Bootland, N., Dolean, V., Graham, I. G., Ma, C. & Scheichl, R. (2022) *GenEO coarse spaces for heterogeneous indefinite elliptic problems*, vol. **145**. Cham: Springer, p. 3.

Bourgeous, A., Bourget, M., Lailly, P., Poulet, M., Ricarte, P. & Versteeg, R. (1991) Marmousi, model and data. *Proceedings of the 1990 EEAG Workshop on Practical Aspects of Seismic Data Inversion* (R. Versteeg & G. Grau eds). Zeist: EAEG, pp. 5–16. Zeist.

Bourquin, F. (1990) Analysis and comparison of several component mode synthesis methods on one-dimensional domains. *Numer. Math.*, **58**, 11–33.

Bourquin, F. (1992) Component mode synthesis and eigenvalues of second order operators: discretization and algorithm. *ESAIM: Math. Model. Numer. Anal.*, **26**, 385–423.

Brown, D. L., Gallistl, D. & Peterseim, D. (2017) Multiscale Petrov-Galerkin method for high-frequency heterogeneous Helmholtz equations. *Meshfree Methods for Partial Differential Equations **115** of Lecture Notes in Computer Science and Engineering* (Griebel, M., Schweitzer, M. eds). Cham: Springer, pp. 85–115.

Buck, M., Iliev, O. & Andrä, H. (2013) Multiscale finite element coarse spaces for the application to linear elasticity. *Open Math.*, **11**, 680–701. Publisher: De Gruyter Open Access.

Chaumont-Frelet, T. & Nicaise, S. (2020) Wavenumber explicit convergence analysis for finite element discretizations of general wave propagation problems. *IMA J. Numer. Anal.*, **40**, 1503–1543.

Chen, Y., Hou, T. Y. & Wang, Y. (2021) Exponential convergence for multiscale linear elliptic PDEs via adaptive edge basis functions. *Multiscale Model. Simul.*, **19**, 980–1010.

Chen, Y., Hou, T. Y. & Wang, Y. (2023) Exponentially convergent multiscale methods for 2d high frequency heterogeneous Helmholtz equations. *SIAM J. Multiscale Model. Simul.*, **21**, 849–883.

Conen, L., Dolean, V., Krause, R. & Nataf, F. (2014) A coarse space for heterogeneous Helmholtz problems based on the Dirichlet-to-Neumann operator. *J. Comput. Appl. Math.*, **271**, 83–99.

Courant, R. & Hilbert, D. (1953) *Methods of Mathematical Physics*, vol. **I**. New York, N.Y: Interscience Publishers, Inc.

Craig, R. R. & Bampton, M. C. C. (1968) Coupling of substructures for dynamic analyses. *AIAA J.*, **6**, 1313–1319.

Deraemaeker, A., Babuška, I. & Bouillard, P. (1999) Dispersion and pollution of the FEM solution for the Helmholtz equation in one, two and three dimensions. *Int. J. Numer. Methods Eng.*, **46**, 471–499.

Efendiev, Y., Galvis, J. & Hou, T. Y. (2013) Generalized multiscale finite element methods (GMsFEM). *J. Comput. Phys.*, **251**, 116–135.

Efendiev, Y. & Hou, T. Y. (2009) *Multiscale Finite Element Methods*. New York, NY: Springer New York.

Erlangga, Y. A., Oosterlee, C. W. & Vuik, C. (2006) A novel multigrid based preconditioner for heterogeneous Helmholtz problems. *SIAM J. Sci. Comput.*, **27**, 1471–1492.

Freese, P., Hauck, M. & Peterseim, D. (2021) Super-localized orthogonal decomposition for high-frequency Helmholtz problems. arXiv: 2112.11368.

Gander, M. J., Loneland, A. & Rahman, T. (2015) Analysis of a new harmonically enriched multiscale coarse space for domain decomposition methods. arXiv:1512.05285.

Giammatteo, E., Heinlein, A. & Schlottbom, M. (2023) Searhein/acms-Helmholtz: Acms-helmholtz v1.0.0.

Gilbarg, D. & Trudinger, N. S. (2001) *Elliptic Partial Differential Equations of Second Order. Classics in Mathematics*. Berlin: Springer-Verlag. Reprint of the 1998 edition.

Gong, S., Graham, I. G. & Spence, E. A. (2020) Domain decomposition preconditioners for high-order discretisations of the heterogeneous Helmholtz equation. *IMA J. Numer. Anal.*, **41**, 2139–2185.

Graham, I. G. & Sauter, S. A. (2019) Stability and finite element error analysis for the Helmholtz equation with variable coefficients. *Math. Comp.*, **89**, 105–138.

Grisvard, P. (2011) *Elliptic Problems in Nonsmooth Domains*. Boston, London, Melbourne: Pitman Publishing.

Gröger, K. (1989) A $W^1$, $p$-estimate for solutions to mixed boundary value problems for second order elliptic differential equations. *Math. Ann.*, **283**, 679–687.

Heinlein, A., Hetmaniuk, U., Klawonn, A. & Rheinbach, O. (2015) The approximate component mode synthesis special finite element method in two dimensions: Parallel implementation and numerical results. *J. Comput. Appl. Math.*, **289**, 116–133.

Heinlein, A., Klawonn, A., Knepper, J. & Rheinbach, O. (2018) Multiscale coarse spaces for overlapping Schwarz methods based on the ACMS space in 2D. *Electron. Trans. Numer. Anal.*, **48**, 156–182.

Heinlein, A., Klawonn, A., Knepper, J. & Rheinbach, O. (2019) Adaptive GDSW coarse spaces for overlapping Schwarz methods in three dimensions. *SIAM J. Sci. Comput.*, **41**, A3045–A3072.

Heinlein, A. & Smetana, K. A fully algebraic and robust two-level Schwarz method based on optimal local approximation spaces, July 2022. arXiv:2207.05559.

Henning, P. & Målqvist, A. (2014) Localized orthogonal decomposition techniques for boundary value problems. *SIAM J. Sci. Comput.*, **36**, A1609–A1634.

Hetmaniuk, U. & Klawonn, A. (2014) Error estimates for a two-dimensional special finite element method based on component mode synthesis. *Electron. Trans. Numer. Anal.*, **41**, 109–132.

Hetmaniuk, U. L. & Lehoucq, R. B. (2010) A special finite element method based on component mode synthesis. *ESAIM: Math. Model. Numer. Anal.*, **44**, 401–420.

Hou, T. Y. & Wu, X. H. (1997) A multiscale finite element method for elliptic problems in composite materials and porous media. *J. Comput. Phys.*, **134**, 169–189.

Hurty, W. C. (1960) Vibrations of structural systems by component mode synthesis. *J. Eng. Mech. Div.*, **86**, 51–69.

Joannopoulos, J. D., Johnson, S. G., Winn, J. N. & Meade, R. D. (2008) *Molding the Flow of Light*. Princeton, NJ [ua]: Princeton Univ. Press.

Lafontaine, D., Spence, E. A. & Wunsch, J. (2022) Wavenumber-explicit convergence of the hp-FEM for the full-space heterogeneous Helmholtz equation with smooth coefficients. *Comput. Math. Appl.*, **113**, 59–69.

Larsson, S. & Thomée, V. (2003) *Partial Differential Equations with Numerical Methods*, vol. **45**. Berlin, Heidelberg: Springer Berlin Heidelberg.

Lions, J. L. & Magenes, E. (1972) *Non-Homogeneous Boundary Value Problems and Applications*. Berlin, Heidelberg: Springer Berlin Heidelberg.

Liu, X., Xia, J., de Hoop & Ou, X. (2022) Interconnected hierarchical structures for fast direct elliptic solution. *J. Sci. Comput.*, **91**, 15.

Ma, C., Alber, C. & Scheichl, R. (2023) Wavenumber explicit convergence of a multiscale generalized finite element method for heterogeneous Helmholtz problems. *SIAM J. Numer. Anal.*, **61**, 1546–1584.

Madureira, A. & Sarkis, M. (2018) Adaptive deluxe BDDC mixed and hybrid primal discretizations. *Domain decomposition methods in science and engineering XXIV, volume 125 of Lect. Notes Comput. Sci. Eng* (Bjørstad, Petter E., Brenner, Susanne C., Halpern, Lawrence, Kim, Hyea Hyun, Kornhuber, Ralf, Rahman, Talal, Widlund, Olof B. eds). Cham: Springer, pp. 465–473.

Målqvist, A. & Peterseim, D. (2014) Localization of elliptic multiscale problems. *Math. Comp.*, **83**, 2583–2603.

McLean, W. C. H. (2000) *Strongly Elliptic Systems and Boundary Integral Equations*. Cambridge: Cambridge University Press.

Melenk, J. & Sauter, S. (2010) Convergence analysis for finite element discretizations of the Helmholtz equation with Dirichlet-to-Neumann boundary conditions. *Math. Comp.*, **79**, 1871–1914.

Melenk, J. M. & Sauter, S. (2011) Wavenumber explicit convergence analysis for Galerkin discretizations of the Helmholtz equation. *SIAM J. Numer. Anal.*, **49**, 1210–1243.

Ohlberger, M. & Verfurth, B. (2018) A new heterogeneous multiscale method for the Helmholtz equation with high contrast. *Multiscale Model. Simul.*, **16**, 385–411.

Peterseim, D. (2017) Eliminating the pollution effect in Helmholtz problems by local subscale correction. *Math. Comp.*, **86**, 1005–1036.

Peterseim, D. & Verfürth, B. (2020) Computational high frequency scattering from high-contrast heterogeneous media. *Math. Comp.*, **89**, 2649–2674.

Shamir, E. (1968) Regularization of mixed second-order elliptic problems. *Israel J. Math.*, **6**, 150–168.

Wang, S., de Hoop, M.V. & Xia, J. (2011) On 3d modeling of seismic wave propagation via a structured parallel multifrontal direct Helmholtz solver. *Geophys. Prospect.*, **59**, 857–873.